

Macroscopic Model of Hypogravity-Induced Primate Brain Activity via Identification and Analysis of a Neurovisuomotor Performance Pathway

Ryan Ellison

Universities Space Research Association

Mona Matar (✉ mona.matar@nasa.gov)

NASA <https://orcid.org/0000-0002-4122-7207>

Suleyman Gokoglu

NASA <https://orcid.org/0000-0002-5649-6565>

Raj Prabhu

Universities Space Research Association

Article

Keywords: visuomotor, spaceflight, brain performance pathway, Artemis, connectome, health and performance, hypogravity, clustering

Posted Date: October 28th, 2022

DOI: <https://doi.org/10.21203/rs.3.rs-2142272/v1>

License: © ⓘ This work is licensed under a Creative Commons Attribution 4.0 International License. [Read Full License](#)

Abstract

During long-duration spaceflight, astronauts will experience gravity-transitions (G-transitions) between Earth-gravity (1G) and hypogravity (gravity < 1G), as well as prolonged time in hypogravity environments (i.e., interplanar, the Moon and Mars). The neural substrate underlying coordinated, volitional visuomotor movements like reach-to-grasp is tuned to produce proper movement in 1G. During G-transitions and hypogravity, the brain's visuomotor control network becomes inadvertently configured through its activity states and interconnections to produce erroneous movements. Thus, the need to identify the brain performance pathways underlying mission-critical behaviors like performing visuomotor tasks and understanding their neurophysiological responses during space travel is critical for astronauts' safety and mission success. This work utilizes a whole-brain, primate connectome to identify a visuomotor subnetwork, using a novel modularity algorithm. The identified visuomotor subnetwork is analyzed using local graph theory measures, suggesting the parietal cortex intraparietal sulcus (PCIP), superior parietal cortex (PCS), and secondary visual cortex (V2) are structurally positioned to play an important role in network activity and function. 1G macroscopic neural network, neural ensemble models are developed and subjected to emulated hypogravity, analyzed using an unsupervised machine learning technique to cluster simulations into hypogravity-affected and -unaffected groups. Qualitative analyses of region-wise frequency distributions and means between groups suggest the cingulate cortex (CCP), PCS, ventrolateral pre-motor cortex (PMCVL), primary visual cortex (V1), and V2 are hypogravity-affected, producing non-normal neural activity in frequency space. Synthesizing the structural and modeling results, this work suggests PCS and V2 may be viable countermeasure targets, ensuring proper visuomotor performance during and after spaceflight.

Introduction

During the Artemis missions that the National Aeronautics and Space Administration (NASA) is planning to the Moon and subsequently to Mars, astronauts will experience changing gravitational effects in the form of gravity transitions (G-transitions) and hypogravity exposure. Astronauts will begin in an Earth gravitational environment for which the brain is tuned (denoted herein as $1G = 9.8 \frac{m}{s^2}$) such that it can produce the proper activity or neural signals that underly or control coordinated, volitional movements. Gravity then transitions from 1G to ranges of hypogravity (defined here as gravity < 1G). During and sometime after this G-transition, the neural substrate that was tuned to produce proper movements is now inadvertently configured through its activity states and interconnections such that the movements it produces are erroneous [1, 2, 3, 4, 5, 6, 7]. Adaptation occurs during prolonged periods of hypogravity exposure [8, 9, 10]. However, re-entrance into an environment with substantially higher gravity (e.g., the Moon or Mars) yet again produces a G-transition that the brain matter must contend with to produce reliable and accurate coordinated, volitional movement. Thus, the need to identify the structural neural networks (i.e., the brain performance pathways) underlying mission-critical behaviors like performing visuomotor tasks and understanding the neurophysiological responses within those neural subnetworks during G-transitions and hypogravity exposure is critical for astronaut safety and mission success [11].

Many methods [12] have been derived from graph theory to separate connectivity datasets like that of whole-brain connectomes into subnetworks called communities or modules. These subnetworks can be thought of as structural building blocks of brain connectivity that are functionally specialized and give rise to rich and complex neural activity, effectuating well-known dynamic states like metastability and synchronizability. More specifically, modules can be defined as clusters of densely interconnected nodes with sparse inter-cluster connectivity [13, 14, 15]. In context of this work, the applicable, previously derived methods can be summarized as structural modularity algorithms, which include partitioning [16, 17, 18, 19, 20, 21, 22] and distance methods [23]. The utility of these specific structural modularity methods seems to be limited.

The desired module in this work is a general subnetwork responsible for the neural control of visuomotor movement such as reach-to-grasp [24, 25, 26, 27, 28, 29, 30, 31, 32, 33]. In a real-world environment, this involves identifying an object in the visual field, reaching towards and grasping said object for manipulation, a sort of brain performance pathway for visuomotor movement. Because this is visuomotor, it encompasses aspects of the visual system and the motor system. Therefore, it is doubtful that already derived structural modularity algorithms using partitioning or distance measures, simply looking for dense connectivity, would work well.

Mesoscopic and local measures of the structural architecture of this connectome using graph-theory measures have been reported [34]. They were achieved using the entirety of the primate connectome dataset. Here, we are concerned with local network measures of the structural visuomotor subnetwork, identifying regions within the subnetwork that are structurally positioned to play an important role in shaping network activity. If nodes, through their connectivity, are structurally significant, they are more likely to be important functionally, and therefore, behaviorally.

The architecture of the structural neural subnetwork, which through its many interconnections produces unpredictable network dynamics, allows for the construction of macroscopic neural models, beginning with the individual components or brain regions of the subnetwork that then become interconnected to produce a full, macroscopic network model. Phenomenological dynamic systems' models have been derived and used to describe neural activity across multiple levels of nervous system organization, from individual neurons [35, 36, 37, 38, 39, 40] to neural masses representing brain region populations [34, 41, 42, 43, 44, 45, 46].

The 2D oscillator, or other low-dimensional models, governing local field potential (LFP) activity of singular brain-region models have been used successfully in macroscopic neural models to describe aspects of resting state brain activity [47, 48]. Resting state brain activity studies form the basis of critical brain theory, which states biological neural networks organize near state transitions, a concept called self-organized criticality [49, 50] and justify the benefits of such modeling efforts.

Even though the 2D oscillatory model has been used to describe fundamental properties of emerging resting state neural dynamics, it has not been used to describe neural activity of active, task-performing behavior such as reach-to-grasp-like visuomotor movement. More generally, using a macroscopic neural network, neural ensemble (NNNE) model comprised of neural masses to describe such behavior has not, to the authors' knowledge, been attempted.

The subjection of the 1G visuomotor model to hypogravity is based on a conceptual framework describing electrophysiological changes of neural substrate in decreased gravity. At a cellular/multicellular level, Kohn and Ritzmann (2018) [51] described a neurophysiological framework indicating that biophysical changes in the neuronal membrane result in an increased resting potential and a decrease in action-potential threshold, which can be summarized as an increase in neuronal excitability, as well as a decrease in conduction velocity and synaptic transmission. The latter can be succinctly described as a decrease in the ability of a neuron to affect its downstream partner. The review by Wuest et al. (2018) [7] described the effects of microgravity across multiple levels of organization, from the cellular membrane to the brain as an organ. At the organ level, there is a decrease in axonal excitability, as well as a decrease in nerve and synaptic conduction velocity. Furthermore, a decrease in intracranial activity is reported, which is the kind of activity modeled here and could be thought of as decreased excitability.

There is agreement between the work done by Kohn and Ritzmann (2018) [51] and the work reviewed by Wuest et al. (2018) [7] with respect to decreased conduction velocity and synaptic efficacy, but there is an apparent conflict between the increase in excitability suggested by Kohn and Ritzmann (2018) [51] and decrease in excitability suggested by Wuest et al. (2018) [7]. However, the conflict can be resolved by re-examining the dominant causation of LFPs. These macroscopic signals are thought to arise largely from post-synaptic potentials [52]. Therefore, even though on a single-cell level there is an increase in excitability, resulting in increased action potential generation, in microgravity there is a decrease in conduction velocity, as well as a decrease in the efficacy of synapses, which would decrease the production of post-synaptic potentials. This results in a decrease in “excitability” as considered here in macroscopic recordings like LFPs.

In this work, we identify from a whole-brain primate connectome a 14-node structural visuomotor subnetwork (i.e., a visuomotor brain performance pathway) using a novel modularity algorithm. We analyze it using local graph theory measures, identifying the intraparietal sulcus of the parietal cortex (PCIP), superior parietal cortex (PCS), and secondary visual cortex (V2) as important structural regions for network activity. We then use the structural visuomotor subnetwork to engineer a macroscopic visuomotor model of LFP brain activity in 1G and subject it to hypogravity using the Wuest et al. (2018) framework [7]. We investigate the neurophysiological responses of brain regions within the neural network that could occur during G-transitions and hypogravity exposure. Using a machine learning algorithm, we cluster the frequency output of 30 disparate 1G visuomotor models subjected to hypogravity into hypogravity-affected and -unaffected groups and qualitatively analyze the region-wise frequencies between these groups. We identify the posterior cingulate cortex (CCP), PCS, ventrolateral pre-motor cortex (PMCVL), primary visual cortex (V1), and V2 as hypogravity-affected. Comparing the regions identified as structurally consequential with those identified through model simulations as being affected by hypogravity, this work suggests regions PCS and V2 contribute to affected visuomotor performance during G-transitions and hypogravity exposure, going from brain adapted to non-adapted states. Thus, these regions may be viable countermeasure targets, ensuring proper visuomotor performance during and after spaceflight.

Results

Identification of visuomotor subnetwork using modularity algorithm

The visuomotor module that results from passing the whole-brain primate connectome to the modularity algorithm is depicted in Fig. 1. The module contains 14 brain regions (Table 1) and 146 long-range interconnections. Due to apparent left-brain specialization for visuomotor function [53, 54, 55, 56, 57, 58], all 14 brain regions and their interconnections are contained to the left hemisphere (Fig. 1a).

Table 1
Abbreviations and expanded names of 14 brain regions in visuomotor module and 4 hand-pruned regions. These regions are all contained within the left hemisphere

Module	Pruned	Region
CCA		cingulate cortex anterior
CCP		cingulate cortex posterior
IP		insula posterior
M1		primary motor cortex
PCIP		parietal cortex intraparietal sulcus
PCM		parietal cortex medial
PCS		parietal cortex superior
PMCDL		premotor cortex dorsolateral
PMCM		premotor cortex medial (supplementary motor cortex)
PMCVL		premotor cortex ventrolateral
S1		primary somatosensory cortex
S2		secondary somatosensory cortex
V1		primary visual cortex
V2		secondary visual cortex
	AMYG	amygdala
	PFCORB	prefrontal cortex orbital
	PFCPOL	prefrontal cortex pole
	TCC	temporal cortex central

The connectivity matrices of the visuomotor module are depicted in Fig. 1. These tract-weight (Fig. 1b) and tract-length (Fig. 1c) are needed to identify structurally significant regions in the visuomotor neural network and are requisites for building a macroscopic model of visuomotor function as they instantiate the biophysical realism of the interplay between brain regions across their interconnecting neural network. The tract-weight matrix (Fig. 1b) is a weighted, directed graph, meaning it has lost the bi-hemispheric symmetry that was present in the full connectome. This is a product of the visuomotor module containing a single hemisphere, as these uni-hemispheric measures are made experimentally to construct the full connectome. More specifically, the representation of reciprocal connectivity in this context results in the observed matrix asymmetry. The tract-length matrix (Fig. 1c) is now a weighted, undirected graph, meaning it now has symmetry. Again, the reduction of the primate connectome to regions of a single hemisphere is the culprit, as the distance between one left-hemispheric region to any other is the same as the distance of any other to one left-hemispheric region.

Local network analysis of structural visuomotor subnetwork

The local network analysis of the visuomotor model is done using three centrality measures (i.e., betweenness (Fig. 2a), closeness (Fig. 2b), and relative degree (Fig. 2c)) and one network resilience measure (i.e., average neighbor degree (Fig. 2d)), allowing for the determination of the most structurally important nodes for proper visuomotor-network activity, function, and resulting behavior. The PCIP had the highest measure across each centrality metric (highlighted in Fig. 2a, Fig. 2b, and Fig. 2c). Thus, the PCIP is the “primary hub” of the visuomotor module. The superior parietal cortex (PCS) also repeatedly scores in the top 25% across centrality measures, specifically in both betweenness and relative degree (highlighted in Fig. 2a and Fig. 2c), identifying it as a “secondary hub” of the visuomotor module. The last brain region that reappears in the top 25% of each centrality measure was V2, in both betweenness and closeness (highlighted in Fig. 2a and Fig. 2b), making it another “secondary hub” of the visuomotor module.

The primary and secondary hubs are then compared to the 25% of nodes scoring lowest on the average neighbor degree network resilience measure. V2, a secondary hub of the subnetwork, has the lowest average neighbor degree (highlighted in Fig. 2d). The primary hub of the visuomotor module, PCIP, has the penultimate lowest average neighbor degree (highlighted in Fig. 2d).

Exploration of brain-region model dynamics

Exploration of the brain-region model begins with a three-dimensional analysis of its bifurcations. The steady-state bifurcation analysis (Fig. 3a top; steady-state bifurcation diagram in grey) is constructed from 199 simulations across different bifurcation parameters, i , in the inclusionary set [0, 20]. At low values, the steady-state of the brain-region model is stable (Fig. 3a top; solid grey line) as it converges to its nodal attractor resulting in an unchanging voltage. As the bifurcation parameter increases, the brain-region model approaches criticality and undergoes a supercritical Hopf bifurcation [59]. The system becomes unstable (Fig. 3a top, dotted grey line), and the voltage variable approaches a new limit-cycle attractor (Fig. 3a top, solid grey line), corresponding to an oscillatory state. Increasing the bifurcation parameter further results in the system again approaching criticality, undergoing a subcritical Hopf bifurcation, where the instability disappears and the system approaches again a stable nodal attract (Fig. 3a, solid grey line), corresponding to an unchanging voltage.

The brain-region model is subjected to a ramping procedure of the bifurcation parameter to analyze the system's instantaneous bifurcations. The instantaneous bifurcation analysis is depicted in Fig. 3a top, color-mapped trace. The system underwent the same bifurcations as in the steady-state bifurcation analysis during the ramping procedure. However, the criticalities that result in activity transitions through supercritical and subcritical Hopf bifurcations are delayed as a function of the bifurcation parameter, a sort of transitional hysteresis [59]. Thus, the system can produce unexpected transitions dependent on the rate at which they are changed. Time-series data of the voltage variable is shown in Fig. 3a bottom.

A 2D phase portrait is used to illustrate the primary activity regimes of the brain-region model. In Fig. 3b top, the steady-state solutions to the differential equations governing the state variables of the brain-region model are illustrated as nullclines [59], a cubic nullcline, which shifts along the y-axis, as well as a linear nullcline. The blue data represents the brain-region model in the quiescent/excitable regime. This is illustrated by a stable node (Fig. 3b top, blue dot), which represents the attractor for the quiescent regime. The blue excursions in the phase portrait represent the excitable regime, where the model is perturbed with positive and negative stimulations. In Fig. 3b bottom, the voltage activity as a function of time is shown for both the quiescent regime (the isoelectric or non-changing blue line) and the excitable regime (small and large voltage excursions of the blue line). The oscillatory regime is also illustrated.

Lastly, the ability of the brain-region model to produce inherent oscillations across a wide range of frequencies, at least those frequencies often observed in LFP recordings, is shown in Fig. 3c. With different parameterizations from the tabulated parameter data, we verify that the model can readily generate oscillatory activity with frequencies 2, 25, and 50 Hz, representing delta, alpha, and gamma ranges.

Visuomotor model in 1G

Figure 4a (data in black) illustrates the 1G data acquired from the literature regarding the macroscopic electrophysiological activity of these brain regions when performing reach-to-grasp-like visuomotor behavior. The dotted lines represent frequency ranges reported in the literature, and the black dots represent dominant frequencies. The majority of the brain regions present in the visuomotor subnetwork produce LFP or LFP-related brain activity (data in blue) in the beta wave range (approximately 12 to 35 Hz). Four regions produce activity in the gamma wave range (> 35 Hz), while two produce slower oscillatory activity in the delta, theta, and alpha ranges (1 to 12 Hz). Thus, the visuomotor neural network, neural ensemble model produces LFP activity in the requisite frequency ranges for a brain in 1G.

Figure 4b shows a 2D representation of the neural network, as well as the corresponding activity of each of the nodes or brain regions within the NNNE model as a function of time.

Analysis of visuomotor model subjected to hypogravity

Figure 5a depicts the clustering of raw frequency data across the entirety of 1G and hypogravity model runs. *De facto* 1G frequency-space simulation data is also included for reference (red lines). Both cluster 1 (blue lines) and cluster 2 (orange lines) show seemingly large variations away from known region-wise 1G model data. Thus, it is not trivial to define these clusters as hypogravity-affected and -unaffected. Also, the high dimensionality makes it difficult to visualize clear clustering. Therefore, soft k-means results are dimensionally reduced using principal component analysis (PCA), and the description of explained variance as a function of dimension or principal component is shown in Fig. 5b. The first dimension (explained variance = 69%) and second dimension (explained variance = 7.4%) account for 76.4% of the variance within the data. Thus, we can view the soft k-means clustering in these two reduced dimensions (Fig. 5c), which makes the separation between groups more apparent.

However, there is not an obvious way to use PCA to compare our known 1G data to these clusters (e.g., by looking for cluster overlap), identifying to which cluster the known 1G data belongs, aiding in cluster definitions as hypogravity-affected or -unaffected. Thus, we qualitatively compare the distributions of each cluster to the distributions of our known 1G data using a box-and-whiskers interquartile range (IQR) analysis, concerning ourselves with the densest 50% of respective, region-wise distributions (Fig. 5d). This allows us to determine, through a region-wise comparison, the overlap of IQR between the two clustered groups and 1G reference data. Comparing the yet-defined clusters to the known 1G data makes clear that cluster 1 (blue data) is the hypogravity affected group, whereas cluster 2 (orange data) is the hypogravity unaffected group. To aid the qualitative distribution analysis, we can quantify the distribution shifts by computing the root-mean-squared error (RMS) between the 1st and 3rd quantiles of each cluster and the 1G reference data, using the supposition that the cluster with the largest error for the respective 50% distribution bounds is the hypogravity-affected group. Figure 5e depicts this analysis utilizing a heatmap-like illustration, which utilizes a size encoding of each heatmap element. Cluster 1, the affected group, produces a large error for the 1st (RMS = 364.90 Hz) and 3rd (RMS = 204.85 Hz) quantiles as compared to cluster 2 (1st quartile, RMS = 0.51 Hz; 3rd quartile RMS = 8.67 Hz), supporting our qualitative distribution analysis of the box-and-whiskers plot.

Moreover, we can repeat the qualitative process, comparing the distributions of our two clusters to identify which brain regions show marked shifts in LFP oscillatory frequency (i.e., which brain regions show distribution shifts outside or approximately outside of the IQR range of the comparative group). V2, PMCVL, PCS, and CCP of the affected group (V2: 1st quartile = 73 Hz, 2nd quartile = 75 Hz; PMCVL: 1st quartile = 24 Hz, 2nd quartile = 26 Hz; PCS: 1st quartile = 26 Hz, 2nd quartile = 29 Hz; CCP: 1st quartile = 74 Hz, 2nd quartile = 74 Hz) show large frequency distribution shifts such that the densest 50% of the distribution lies outside or approximately outside of the IQR of the unaffected group (V2: 1st quartile = 69 Hz, 2nd quartile = 73 Hz; PMCVL: 1st quartile = 20 Hz, 2nd quartile = 24 Hz; PCS: 1st quartile = 24 Hz, 2nd quartile = 27 Hz; CCP: 1st quartile = 6 Hz, 2nd quartile = 10 Hz), increasing their frequency output in hypogravity. Contrarily, V1 (hypogravity affected: 1st quartile = 42 Hz, 2nd quartile = 68 Hz; hypogravity unaffected: 1st quartile = 66 Hz, 2nd quartile = 69 Hz) shows a significant distribution shift in the decreasing-frequency direction.

Figure 5f shows the k-means determination, looking at mean LFP frequency data. Again, through a qualitative comparison of means (i.e., looking for means of the affected group that fall outside or approximately outside the standard deviation bars of the unaffected). This qualitative approach identifies nearly identical regions as the box-and-whiskers qualitative analysis. V2, PMCVL, PCS, and CCP show marked increases in average frequency between hypogravity-affected (V2: $\mu = 74.04 \pm 0.50$ Hz; PMCVL: $\mu = 25.32 \pm 0.86$ Hz; PCS: $\mu = 27.10 \pm 1.12$ Hz; CCP: $\mu = 74.00 \pm 0.00$ Hz) and hypogravity-unaffected (V2: $\mu = 70.78 \pm$

1.19 Hz; PMCVL: $\mu = 22.38 \pm 1.50$ Hz; PCS: $\mu = 25.57 \pm 1.19$ Hz; CCP: $\mu = 8.00 \pm 1.43$ Hz) groups. V1, in this analysis, shows a rather large decrease in its mean frequency. However, its standard deviation bars are rather large, encompassing the entirety of the mean and standard deviation of the unaffected group.

Discussion

Using a whole-brain, primate connectome, we identify a 14-brain-region visuomotor subnetwork utilizing a novel modularity algorithm. Local graph theory analyses of said subnetwork suggest PCIP, PCS, and V2 are structurally significant regions that shape network activity, and thus, network function and resulting behavior. A macroscopic visuomotor model (i.e., a NNNE model) is built on top of the 14-brain-region structural visuomotor subnetwork that produces 1G LFP data, which is then subjected to hypogravity utilizing the Wuest et al. (2018) framework [7]. A soft k-means algorithm is used to cluster 30 different 1G visuomotor models into hypogravity-affected and -unaffected groups. These groups are qualitatively analyzed, resulting in the identification of CCP, PCS, PMCVL, V1, and V2 as hypogravity-affected.

Important regions, some non-obvious, captured by the modularity algorithm

The brain regions in the visuomotor subnetwork identified by the modularity algorithm are cortically diffuse. Aside from those which have obvious roles in visual and motor function (e.g., V1; V2; several premotor cortices, PM*; and M1), other notable brain regions, identified as being integral to successful visuomotor/sensorimotor behavior, are captured (see Fig. 1; Table 1). For example, the PCIP, an area found between more anterior somatosensory/motor regions and more posterior visual regions, has been identified as being integral in transforming sensory information into motor information used for motor planning, particularly for arm and eye movements in macaque monkeys [60]. The inner perisylvian region in macaques and humans, which contains S2 and the posterior insular cortex (IP), has been implicated as a sensorimotor integration area activating before and during hand manipulation, hand-target contact, finger exploration, and precision grasping [61]. Lastly, the cingulate cortex has been implicated in the interpretation of outcome information for a present task to guide subsequent action selection. This cortical region contains the anterior cingulate cortex (CCA), which is comprised of three motor areas at least one of which that receives inputs from adjacent motor areas and the prefrontal cortex and all of which directly connect to M1, making it suitable for motor action selection when confronted with stimulus-task-reward behaviors [62].

Thus, the identification of these brain regions, some non-obvious, in the visuomotor network underlying visuomotor task performance highlights regions each of which are integral for some aspect of visuomotor control. Therefore, the activity of these regions should be considered when analyzing the structural integrity of neural networks underlying or controlling visuomotor behavior and how macroscopic electrophysiological activity changes when the brain is subjected to hypogravity.

Regions structurally positioned to play an important role in the function

PCIP is identified as the primary hub of the structural visuomotor subnetwork and scored penultimately low on the local resilience measure (Fig. 2). Thus, it is positioned structurally to shape information flow throughout the network and compromise network activity and function. PCIP is considered part of the dorsal stream of visual information and the interface between the visual system identifying where objects are for manipulation and the motor system using the transformed visual information to plan and execute the manipulative action [63].

The local network analysis identifies the PCS as a secondary hub of the visuomotor subnetwork (Fig. 2). This particular region has been shown through tracer studies to have afferent projections from regions in the dorsal visual stream of information (e.g., the medial bank of the PCIP), parietal areas (e.g., different subregions of the PCS) and frontal motor association, premotor, and M1 areas, as well as from insular and cingulate areas, suggesting a role in goal-directed motor movement like arm movement and motor coordination [64, 65].

Lastly, V2 is identified as another secondary hub and is the region scoring lowest on the local resilience measure, making this region critical for overall network function (Fig. 2). This is supported with histological studies of V2 projections in the macaque, which shows V2 efferent projections back to V1, creating a reciprocal connection, but feed-forward projections to V3, V4, and the middle temporal visual area, as well as medial superior temporal, parieto-occipital, and ventral intraparietal areas, showing the diffuse connectivity to regions in both functionally specific visual streams of information [66].

Thus, the centralities suggested by the local network analysis (Fig. 2), moving in the direction of effective connectivity for the integration of visuomotor information, is a visual subsystem interfacing node (V2), a predominate visuomotor node between the visual and motor system (PCS), and a brain system interfacing node between the visual and motor systems (PCIP). These brain regions are structurally positioned to alter network activity and therefore function, because of brain activity changes, that may result with hypogravity exposure.

Regions identified as hypogravity-affected in NNNE visuomotor model

Literature on the effect of hypogravity on LFP neural activity in primates is, to the authors' knowledge, non-existent. Moreover, there is little literature on human EEG studies in hypogravity, from which comparative insights could potentially be made, as the reviews by Marusic et al. (2014) [67] and Wuest et al. (2018) [7] make clear. To make matters worse, frequency band analysis of EEGs recorded in hypogravity, as defined in this work, have revealed controversial results (Wuest et al., 2018) [7]. A region-wise comparison between the hypogravity modeling results and published experimental data is non-trivial. Thus, a functional analysis of the regions identified as hypogravity-affected can at best allow for inferences about potential dysfunction given hypogravity-driven changes in brain-region activity of the visuomotor control network.

CCP is identified as a hypogravity-affected brain region, one that significantly increases its oscillatory frequency when subjected to this space stressor (Fig. 5). The CCP is involved in many intrinsic control networks in the brain. Its dominant functional role is in the default mode network (DMN) [68, 69, 70]. However, the CCP shows interconnectivity and DMN-anti-correlated activity with other intrinsic control networks, such as the dorsal attention network responsible for top-

down control of externally focused, visual attention [71] and the frontoparietal control network (FPCN) [72], which contains motor-relevant interconnections [73]. Lastly, fractionation of the CCP shows subregions echo many well-defined control networks [74], showing selective functional connectivity with other networks like a sensorimotor network [73, 75]. All of this taken together suggests, with respect to visuomotor movement, the CCP could play a role in the visual attention required to perform a task, in information transformation from visual to motor, and in executive control of motor responses.

The regions PCS and V2 are also identified as being hypogravity-affected, each increasing their frequencies when subjected to emulated hypogravity in the model (Fig. 5). An anatomical analysis is performed in the above discussion subsection Regions structurally positioned to play an important role in function. However, functionally, the PCS is suggested to play a role in goal-directed motor movement like arm movement and motor coordination [64, 65]. More specifically, the PCS responds to the preparation of directed movement, direction of movement, and dynamic position of the hand, as well as to the integration of relevant hand-eye movement for visuomotor coordination [76, 77, 78]. V2 has been shown to be important in the rate of visual learning [79] of which spatial working memory [80] is a part. Spatial working memory is integral for visuomotor adaptation [81, 82], in which V2 may play a role.

PMCVL is another region identified as being hypogravity-affected, also increasing its frequency in the hypogravity-subjected NNNE model (Fig. 5). With respect to reach-to-grasp-like movement, this brain region has been shown to underly visual-to-motor transformation of spatial characteristics of the object to be grasped by the hand into appropriate motor commands [83, 84, 85, 86, 87], writing the source code, if you will, for the primary motor cortex to which it has direct interconnectivity [88, 89, 90, 91] for motor-movement execution.

Lastly, V1 shows altered activity in the NNNE model when subjected to hypogravity, decreasing its frequency (Fig. 5). This region is the first visual processing center of the cortex, receiving feedforward information from the retina, which is passed to the lateral geniculate nucleus of the thalamus [92]. V1 is responsible for simple visual-field computations of basic features, contributing to conscious visualization by its feedforward connectivity to higher visual cortices which integrate these simple characteristics, creating a rich neural representation of the observed environment [93, 94].

Combining the above functional analyses of each region identified as hypogravity-affected by the NNNE model subjected to hypogravity, we can identify potentially vulnerable top-down, cortically controlled functions (Fig. 5). Moving in the direction of effective connectivity, alterations in the neural activity of V1 puts at risk simple visual-field-feature computation and visual-information-gateway function. Hypogravity could potentially alter the rate at which an astronaut can visually learn a task, effecting visuomotor adaptation. Hypogravity could alter PCS's ability to perform visuomotor transformations necessary for goal-directed motor movement like arm movement and motor coordination. Hypogravity-modulated neural activity could alter visual attention and visuomotor transformation. And lastly, PMCVL's function of visuomotor transformation of spatial characteristics, aiding in the planning of motor commands passed to the primary motor cortex, could be jeopardized.

Limitations of current work

Beginning with the structural work of this research, a potential limitation is the resolution of the whole-brain, primate connectome, which contains 76 brain regions. With respect to the identification of a visuomotor subnetwork, utilizing the novel modularity algorithm, a connectome parcellated with such dearth in number of regions makes possible that significant structural regions and interconnectivity are missed.

However, increased connectome granularity would present further difficulty in building a macroscopic NNNE model to simulate neural activity. In this work, 1G frequency data for each brain region included in the model was acquired from literature focused on reach-to-grasp-like movements of monkeys and humans. The literature with these constraints is limited. Thus, increased connectome resolution would imbue in the model significant unknowns. The desired connectome resolution for this work is one with tractability, like the whole-brain, primate connectome that we use.

Another potential limitation of this work is the generic 2D oscillator brain-region model used as the neural masses in the NNNE model. This brain-region model is a classical, phenomenological dynamical systems' model, derived from the observed dynamics of the more biophysically realistic case. Therefore, the model formalism lacks implicit biophysical realism, which decreases its neurophysiological interpretability.

A difficulty that arises when doing computational modeling of systems subjected to aspects of space environment, particularly of this work modeling a neural system with gravity-dependent parameters, is the unknown dependency. Here, there are three gravity-dependent parameters that correspond to neural changes as described in the Wuest et al. (2018) [7] framework. However, we don't know to what gravitational levels discrete values of each parameter correspond. We only know in what direction each parameter tends. Thus, we don't have a transfer function that maps gravitational states to a place in the three-dimensional, gravity-dependent parameter space, $f(G) \rightarrow \{i, c, w\}$.

Synthesizing results from structural and dynamic modeling work

The visuomotor subnetwork, identified from the application of the modularity algorithm to the whole-brain, primate connectome, is analyzed using local graph theory measures. These analyses suggest that PCIP, PCS, and V2 are important structural regions, having an interconnectivity within the visuomotor subnetwork that makes them critical regions for network activity and thus function. The NNNE model, predicated on the structural characteristics of the visuomotor subnetwork, is simulated across many 1G parameterizations, each of which are subjected to the hypogravity framework suggested by Wuest et al. (2018) [7]. This data is then passed to an unsupervised machine learning pipeline, utilizing a soft k-means algorithm, that resulted in the clustering of the 1G and hypogravity model frequency data into hypogravity-affected and hypogravity-unaffected groups. The qualitative analyses of these groups, comparing the frequency distributions and mean frequencies, suggest that CCP, PCS, PMCVL, V1, and V2 are hypogravity-affected regions (i.e., their neural activity markedly changes because of emulated hypogravity). Synthesizing these results, the brain regions suggested to be important by the structural analysis and the brain regions that appear to change their activity in the model when subjected to hypogravity, imply PCS and V2 contribute to affected visuomotor performance during G-transitions and hypogravity exposure. Therefore, these regions may be viable countermeasure targets, ensuring proper visuomotor performance during and after spaceflight.

Materials And Methods

An overview of the computational and analytical workflow is depicted in Fig. 6.

Primate connectome data

The Virtual Brain (TVB) simulation platform pre-packages a macroscopic connectivity dataset of a primate brain [34, 95]. This dataset contains 76 cortical brain regions (Appendix Table 1), represented as nodes, and 1,560 long-range, interregional connections like that of corticocortical connections, commissural fibers, and association tracts represented as edges. The nodes of this connectome are spatially discretized, as opposed to a vertex-based mesh used to model a cortical surface, and represent the three-dimensional centers of mass of each brain region. Figure 7a depicts the brain regions present in the connectivity dataset, illustrating the spatiality and granularity of nodes throughout the brain.

Biophysical characteristics of the connectome edges are represented by two, 76 x 76 square matrices: the tract-weight matrix (Fig. 7b) and the tract-length matrix (Fig. 7c). As described in Leon et al. [34, 95], the weight matrix, indicating the strength of interregional connections, is based primarily on data from the CoCoMac database [96, 97, 98], a relational database collating approximately 40,000 experimental tract-tracing findings regarding the connectomics of the macaque brain [99]. The length matrix, which describes the interregional fiber lengths, is primarily determined by diffuse spectral imaging studies.

The tract-weight data acquired from the CoCoMac database are uni-hemispheric. As such, this aspect of the dataset is made bi-hemispheric by duplicating weights for the contralateral hemisphere. In this matrix, the second and third quadrants represent high-density non-symmetric connectivity intra-hemispherically, whereas the first and fourth quadrants represent bidirectional sparse connectivity inter-hemispherically as seen in Fig. 7b. However, fiber-length determinations are bi-hemispheric, which captures the inherent asymmetries across the midline of the brain [100, 101, 102, 103], and the tract-length matrix is weighted and non-symmetric, as seen in Fig. 7c [95].

Structural visuomotor subnetwork

Modularity algorithm used to identify a visuomotor subnetwork

Visual sensory information is transduced at the retina of the eye, which is communicated via the optic nerve to the lateral geniculate nucleus of the thalamus. Once integrated, visual information leaves the thalamus and travels to V1, the first cortical brain region along this pathway contained in the primate connectome, via the geniculostriate pathway. Visual information is then further processed downstream by V2 and moves along the motor-relevant dorsal visual pathway to eventually terminate in the primary motor cortex (M1) [92].

Using this neurobiological knowledge, we derive a modularity algorithm to identify a visuomotor subnetwork from the entirety of the connectome. We define M1 as the output node and V1 as the input node of the desired visuomotor module, and then, reverse engineer the subnetwork. The algorithm begins at M1 (Fig. 8a) and unpacks a single layer of the connectivity data, where a layer consists of upstream nodes connected to the node being considered. The algorithm checks for the presence of the V1 and unpacks another layer of connectivity data if the input node is not present in this layer.

The algorithm (pseudocode in Appendix) is modularized into multiple functions. An initialization function (Appendix Fig. 1) unpacks the first layer of tract-weight matrix starting from the output node and wrangles it. Another function (Appendix Fig. 2) handles further unpacking of the connectivity data. Unpacking each layer involves an iterative process of identifying the row (targets) corresponding to the sources of the resulting initialized dataframe (unpacking a second layer) or the second layer dataframe (unpacking a third layer).

Once the algorithm detects the presence of the input node, it disregards all nodes in that layer (Fig. 8b) and begins at the input node to trace all possible paths back to the output node. For the primate connectome, we restrict the number of steps it can take to 20, which once passed, produces unrealistic results.

After path tracing is complete, we implement a result-driven and hard-coded pruning procedure to remove nodular and edge redundancies. Because of an apparent left-brain visuomotor lateralization [53, 54, 55, 56, 57, 58], we also remove right-brain regions that could have resulted from colossal connections, if they are present. Lastly, the algorithm is ignorant of brain-region function. We cross-reference the resulting module's brain regions with work identifying brain regions responsible for motor, visual, and visuomotor function [104, 105, 106, 107], and perform a qualitative functional analysis which results in a hand-coded pruning of four regions (Table 1).

A rebuild function (Appendix Fig. 3) is responsible for tracing all possible paths from the input node back to the output node. The function begins with unpacking the connectome to its second layer of source nodes. With a control loop constraining the number of possible steps the rebuild method can take (steps = 20), this method firstly filters the dataframe that results from unpacking, identifying the input node as a source and iteratively determining its targets that are not the output node as the new set of sources. This process results in the visuomotor module, which is subjected to data-driven pruning of duplications and colossal, right-hemispheric connections and a hand pruning of regions.

Graph-theoretic measures for local subnetwork analysis

To analyze the local network, we employ three centrality measures identifying important nodes that are well positioned to play a pivotal role in network activity, and a single local network resilience measure, identifying regions that imbue network-activity vulnerability [108].

Betweenness

Betweenness centrality calculates the fraction of all shortest paths that contain a given node in a network. Thus, nodes interfacing different paths in a network have higher betweenness metrics [109].

Closeness

Closeness centrality indicates the distance between a given node and all other nodes in the network and is often defined as the inverse of the average shortest path length of said node to every other node [111, 110]. Thus, the smaller the average path-length the higher the centrality measure as it is structurally positioned less distant to all other nodes.

Relative degree

The degree of a node is the total number of edges connected to it irrespective of direction (). Relative degree measures the number of outgoing connections relative to the number of incoming connections as () [108].

Average neighbor degree

Average neighbor degree is a local assortativity measure, which suggests the degree to which a network is vulnerable to perturbation or disruption. It provides hints as to which regions may compromise network function if perturbed, injured, or otherwise change their activity [108].

We apply each of the connectivity metrics described above to the visuomotor subnetwork's 14 x 14 tract-weights matrix (Fig. 1b). The interpretation of the results of the local network analysis begins with identifying the nodes scoring highest on the three centrality measures (i.e., betweenness, closeness, and relative degree). Here we take the top 25%, that is 4 of the 14 nodes in the visuomotor module. For relative degree, we choose to focus on those nodes whose scores are at or around 0, as these nodes have equal chance to be perturbed by incoming connections or perturb downstream nodes through outgoing connections. Only those nodes that score in the top 25% of two or more centrality metrics are considered. These nodes are then cross-referenced with the 25% of nodes scoring lowest on the network resilience measure (i.e., the average neighbor degree), as centralities scoring lowest on average neighbor degree correspond to nodes that, when perturbed, damaged, or otherwise change their activity, may result in abnormal network activity [108] and thus, the function or behavior the network underlies.

Macroscopic visuomotor model

Brain-region model

In this work, a generic 2D oscillator describes the population activity of a singular brain region, ascribed to each node of the structural visuomotor module, representing their average voltage activity (i.e., the deterministic LFP activity). The brain-region model can be expressed mathematically as:

$$v_i = V(v, u) = d\tau(-fv^3 + ev^2 + gv + \alpha u + \gamma i)$$
$$u_i = U(v, u) = \frac{d}{\tau}(cv^2 + bv - \beta u + a)$$

where $V(v, u)$ represents the average population voltage activity, and $U(v, u)$ a relatively slow resetting state variable that allows oscillatory activity to occur. A notable parameter in this work is i in $V(v, u)$, which represents the excitability of a brain region and used in the exploration of the model as its bifurcation parameter. A detailed description of each parameter can be found in Leon et al. (2015).

Random parameter search and tabulation

We conduct a random parameter search for the brain-region model and tabulate the frequencies and corresponding parameter sets. Each parameter in the brain region model is subset to exclusionary ranges ($a \in (-5, 5)$, $b \in (-20, 10)$, $c \in (-10, 10)$, $d \in (0.0001, 1)$, $e \in (-5, 5)$, $f \in (-5, 5)$, $g \in (-5, 5)$, $\alpha \in (-5, 5)$, $\beta \in (-5, 5)$, $\gamma \in (-1, 1)$, $i \in (-\epsilon, \epsilon)$), allowing for a rich repertoire of dynamic states and activity profiles, as denoted by the TVB simulation platform [95]. The brain-region model is then simulated for $n_{simulations} = 15,000$ runs (chosen to produce many parameter sets per frequency), simulated for $t = 5$ seconds (chosen to ensure resulting voltage transients can converge to steady-state activity) with a time step $\Delta t = 0.02$ ms (chosen to decrease computational cost across $n_{simulations}$).

For each simulation of the model, the parameter ranges denoted above are continuously and uniformly distributed, and each parameter is randomly selected. The voltage activity for the final second of simulated time is Fourier transformed, and the maximum of the magnitude spectrum determines the dominant frequency. The dominant frequency and corresponding parameter set are tabulated if the frequency f , in Hz, is $2 \leq f \leq 100$. The random parameter search results in 13,821 tabulated parameter sets and their corresponding frequencies.

Exploration of brain-region model

The qualitative theory of dynamic systems [112] is used to explore the brain-region model. A three-dimensional bifurcation diagram is constructed using the brain-region model's state variables, $V(v, u)$ and $U(v, u)$, and the bifurcation parameter, i . The model is simulated under two schemes, a ramping scheme and a steady-state scheme. For the ramping scheme, the model is firstly simulated to steady state across a singular run for $t = 5$ s with a time step $\Delta t = 0.025$ ms, with the default parameterization as indicated by the TVB simulation platform [95] (see parameterizations below). The 5 s simulation time is sufficient for the model to reach steady state as the default parameterization produces quiescent voltage activity. The values of the state variables at $t = 5$ s from this simulation are used as the initial conditions at $t = 0$ s for the ramping simulation ensuring the model begins on its stable attractor. The ramping simulation is run for the same time with the same time step. The bifurcation parameter is then vectorized such that $i = [0, 20]$, where the length of the vector equals the length of the simulation, $\frac{t}{dt}$. This results in a singular discretized simulation that can be visualized in three dimensions.

For the steady-state scheme, the model is simulated for $t = 30$ s with a time step $\Delta t = 0.025$ ms. This longer time is used to ensure a true steady state can be achieved with each simulation across many bifurcation parameters as the model produces different types of voltage activity. The vectorized bifurcation parameter used in the ramping scheme is sequenced from 0 to 20, taking every thousandth instance. The model is then simulated iteratively over each bifurcation parameter resulting in $n_{simulations} = 199$ runs, where the final 1 s of data is captured. The minimum and maximum of each state variable for each steady-state run of the brain-region model is determined across each bifurcation parameter. This results in many sets of $\{v_{min}, v_{max}, u_{min}, u_{max}, i\}$. When $v_{min} = v_{max}$ and $u_{min} = u_{max}$, the model is quiescent, in a state where the model is at its stable attractor. When $v_{min} \neq v_{max}$ and $u_{min} \neq u_{max}$, the model reaches criticality and bifurcates, and thus, a new attractor emerges.

The brain-region model is then simulated across many selected bifurcation parameters showcasing primary model regimes using its 2D phase plane: the quiescent/excitable, oscillatory, and hyperexcited regimes. For each simulation the model is run for $t = 5$ s with a time step $\Delta t = 0.025$ s. The quiescent/excitable regime is captured in the model using the default parameterization (see parameterization below). The voltage activity for the final 1 s of each simulation is captured. To uncover the model's excitability, we implement positive and negative stimulations in the model through the bifurcation parameter, $i_{tot} = i + i_{stim}$. The oscillatory and hyperexcited regimes are simulated by setting the bifurcation parameter to 10 and 20, respectively.

To illustrate the brain-region model's ability to generate activity at a wide range of inherent oscillatory frequencies, we simulate the model with the parameters in Table 2, randomly selected at 2 Hz (delta range), 25 Hz (alpha range), and 50 Hz (gamma range). For each simulation the model runs for $t = 5$ s with a time step $\Delta t = 0.025$ s. A 2nd-order Runge-Kutta integrator is used across all exploratory simulations of the brain-region model.

Table 2
Parameter sets used in the exploration of
the brain-region model at various
frequencies

	2 Hz	25 Hz	50 Hz	Default
a	-4.54	2.51	-3.52	-2.00
b	-7.65	13.91	13.86	-10.00
c	4.34	-0.68	0.34	0.00
d	0.0033	0.034	0.054	0.02
e	0.34	-3.31	3.01	3.00
f	2.52	3.24	1.26	1.00
g	3.82	1.14	0.074	0.00
a	3.94	-2.22	-2.90	1.00
β	-3.52	-3.66	-1.21	1.00
Υ	0.24	0.44	0.25	1.00
i	1.52	1.18	-1.95	0.00
τ	4.84	2.42	1.21	1.00

Neural network, neural ensemble model

To instantiate the visuomotor NNNE model, the brain-region model representing the average voltage activity of singular regions must incorporate the connectivity data that comprises the structural neural subnetwork, connecting regions together such that the long-range interregional connections communicate information in the form of voltage to their interconnecting partners. It is this interconnection that constitutes a neural ensemble of regional models. To do this, a linear connectivity equation is used, which can be described mathematically as:

$$\eta_i = g \sum_j w_{ji} v_j \left(t - \frac{d_{ji}}{c} \right)$$

where g is the global coupling parameter, w_{ji} represents the weight of the interconnection from the j^{th} source region to the i^{th} target region from the weight matrix, v_j the average voltage of the j^{th} source region, and $t - \frac{d_{ji}}{c}$ represents the time delay of the effect of the interconnection from the j^{th} source region to the i^{th} target region. In the time delay term, d_{ji} is the length of the interconnection between the j^{th} source region to the i^{th} target region from the length matrix and c is the conduction velocity equal to 5 m/s, which is in the physiologically realistic range for an adult primate [47, 113].

The brain-region model, specifically $V(v, u)$, was then recapitulated to consider the connectivity equation described above. This equation constitutes what is often called a neural mass equation and can be represented mathematically as:

$$v_i = V(v_i, u_i) + \eta_i$$

where v_i represents the average voltage activity of the i^{th} brain region, $V(v_i, u_i)$ represents the fast state variable of the brain region model, which takes into account the slow, resetting state variable $U(v_i, u_i)$ of the i^{th} brain region, and η_i represents additively all of the interconnectivity from the j^{th} source region that affects the i^{th} target region.

1G visuomotor model

To construct a visuomotor NNNE model representing macroscopic (i.e., LFP) brain activity in 1G, frequency data of each brain region in the visuomotor subnetwork is acquired from the literature describing such measurements of monkeys and humans when performing reach-to-grasp-like movements [24, 25, 26, 27, 28, 29, 30, 32, 33]. Frequency data for 11 of the 14 brain regions of the visuomotor subnetwork is found and reported in the literature as dominant frequencies and/or frequency ranges, both of which are recorded. For the three remaining regions (the posterior cingulate cortex, the posterior insular cortex, and the secondary somatosensory cortex), frequency data of macroscopic electrophysiological measurements are taken from available literature [114, 115, 116] to ensure these regions are in an active, synchronous state.

The dominant frequencies, or if ranges are only reported the approximate average of the frequency range, of each brain region are used as input to a Monte Carlo sampling procedure. The dominant/average frequency, f , is used to subset the parameter data that results from the random parameter search in the range $f \pm 3Hz$. This subset data is then randomly sampled, producing 14 parameter sets that, with the brain-region model, produces LFP oscillatory activity for each brain region with the dominant frequency or in the frequency range that is observed when an animal is performing a reach-to-grasp-like visuomotor movement.

These parameter sets are then used in the visuomotor NNNE model. The global coupling parameter of the connectivity equation is iteratively increased until integration failure to ensure the strongest possible network effects as neural networks are often strongly coupled [117, 118], especially those underlying conscious, focused cognition or behavior. The model is then simulated for $t = 5$ s with a time step $\Delta t = 0.00005$ ms with a 4th -order Runge-Kutta integrator, ensuring integration accuracy and stability in a stiffer system.

Hypogravity framework and subsection of 1G visuomotor model

The framework described by Kohn and Ritzmann (2018) [51] and Wuest et al. (2018) [7] identified three neurophysiological features (excitability, conduction velocity, and synaptic efficacy) that change in microgravity. In the visuomotor model, there is an excitability parameter, i , which can be decreased to reflect the decrease in intracranial activity. There is a conduction velocity parameter, c , which can be decreased to reflect the changes in microgravity, as well as a weight matrix, w , governing the efficacy of interregional connections or the effect of a brain region's interconnecting fibers on its downstream partners. Thus, there is a three-dimensional parameter space that we can alter in the direction of decreasing gravity.

We construct a sparse three-dimensional grid across the three parameters/matrix, decreasing 0% (1G value), 25%, 50%, and 75% of their 1G-model value. The implementation of hypogravity begins with a visuomotor-model simulation in 1G and is then iteratively simulated across the sparse grid considering every combination of the hypogravity-inducing parameters.

Because we are using a phenomenological brain-region model, and in order to capture the dynamic state of an active NNNE model underlying visuomotor behavior, we perform the Monte Carlo sampling of the parameter data for each region 50 times, resulting in 50 parameter sets for a visuomotor model in 1G. This allows for the simulation of 50 visuomotor models with different dynamic states. Each of these visuomotor models is subjected to the hypogravity procedure described above, resulting in $n_{simulations} = 3,200$, where 50 of those represent visuomotor models in 1G and 3,150 represent visuomotor models in <1G. The activity of each brain region in the visuomotor subnetwork is then Fourier transformed. The resulting frequency data are preprocessed, removing simulation instances that yield non-oscillatory activity, resulting in a dataset consisting of 30 visuomotor models and 1,976 frequency sets (30 with 1G parameters and 1,946 with hypogravity parameters).

Clustering of 1G and hypogravity-subjected models

To analyze the effects of hypogravity on the activity of the visuomotor NNNE model, we implement a fuzzy k-means (FKM) unsupervised machine learning algorithm [119] to cluster the activity of the visuomotor model into hypogravity-affected and -unaffected groups. The visuomotor model's 14 brain regions are used as input features to the FKM algorithm, where each feature vector consists of frequency data across all 14 regions of the NNNE model. The pre-specified number of desired clusters is $k = 2$, as we have two visuomotor models producing LFP activity, one with 1G and the other one with <1G parameterizations. Thus, the presumption is that these 1G visuomotor models oscillating at frequencies determined from literature would cluster with parameterizations thought to be hypogravity-inducing and producing relatively similar activity. The clustering results in hypogravity-affected and -unaffected groups allowing for further region-wise frequency comparisons identifying brain regions that produce abnormal activity.

The algorithm works using a centroid method, minimizing the sum-of-squares distance function within cluster. The number of iterations allowed for cluster assignment and centroid update is 10^6 to ensure true convergence of the clusters as the algorithm exits after minimization [119].

Declarations

DATA AVAILABILITY

Data is publicly available and can be freely downloadable from The Virtual Brain at <https://www.thevirtualbrain.org>.

CODE AVAILABILITY

All code developed for this work can be obtained with a reasonable request to the NASA affiliated authors and after appropriate government export control review.

ACKNOWLEDGEMENTS

The authors are grateful for the support of NASA's Human Research Program, especially the CBS portfolio for the many discussions throughout the research.

COMPETING INTERESTS

The authors declare no competing interests.

AUTHOR CONTRIBUTIONS

M.M. conceived the project, searched literature, identified dataset, supervised the methods and analyses, led discussions, and contributed to editing the manuscript. R.E. searched literature, acquired the datasets, designed and implemented all aspects of the modeling, performed analyses, derived the results, and wrote the initial draft of the manuscript. S.A.G. and R.K.P. guided logistic planning, supervised the development and interpretation of the results, and contributed to editing of the manuscript.

References

1. Gazenko, O. G., Genin, A. M., and Yegorov, A. D. (1981). Summary of medical investigations in the USSR manned space missions. *Acta Astronaut.* 8, 907–917. doi: 10.1016/0094-5765(81)90061-8
2. Groen, E., Clarke, A., Bles, W., Wuyts, F., Paloski, W., et al. (2007). Physiological Targets of Artificial Gravity: The Sensory-Motor System. In: Clément, G., Buckley, A. (eds) *Artificial Gravity*. The Space Technology Library, vol 20. Springer, New York, NY. doi: https://doi.org/10.1007/0-387-70714-X_4
3. Johnson, R. S., Dietlein, L. F., and Berry, C. A. (1975). *Biomedical Results of Apollo*. Washington, D.C.: NASA.
4. Nicogossian, A. W., Leach-Hunton, C., and Pool, S. L. (1989). *Space Physiology and Medicine*. Philadelphia, PA: Lea and Febiger.
5. Thornton, W. E., and Rummel, J. (1977). "Muscular deconditioning and its prevention in space flight," in *Biomedical Results of Skylab*, eds R. S. Johnston and L. F. Dietlein (Washington DC: NASA), 191–197.
6. White, O., Clement, G., Fortrat J.O., Pavy-LeTraon, A., Thonnard, J.L., et al. (2016). Towards human exploration of space: the THESEUS review series on neurophysiology research priorities. *NPJ Microgravity*, 2, 16023. doi: <https://doi.org/10.1038/npjmgrav.2016.23>
7. Wuest, S.L., Gantenbein, B., Ille, F., and Egli, M. (2018). Electrophysiological experiments in microgravity: Lessons learned and future challenges. *NPJ Microgravity*, 4, 7. doi: <https://doi.org/10.1038/npjmgrav.2016.23>
8. Goswami, N., White, O., Blaber, A., Evans, J., J.W.A. van Loon, J., et al. (2021). Human physiology adaptation to altered gravity environments. *Acta Astronautica*, 189, 216–221. doi: <https://doi.org/10.1016/j.actaastro.2021.08.023>
9. Sijder, R., Mulavara, A., Bloomberg, J.J., and Peters, B.T. (2015). Individual predictors of sensorimotor adaptability. *Front. Syst. Neurosci.*, 9:100, doi: 10.3389/fnsys.2015.00100
10. White, O., Gaveau, J., Bringoux, and Crevecoeur, F. (2020). The gravitational imprint on sensorimotor planning and control. *J. Neurophysiol.*, 124, 4-19. doi: 10.1152/jn.00381.2019
11. Steinberg, S.L. (2019). Human Research Roadmap. <https://humanresearchroadmap.nasa.gov/>
12. Fortunato, S. (2010). Community detection in graphs. *Phys. Rep.*, 486, 75-174. <https://doi.org/10.1016/j.physrep.2009.11.002>
13. Arenas, A., Diaz-Guilera, A., and Perez-Vicente, C.J. (2006). Synchronization reveals topological scales in complex networks. *Phys. Rev. Lett.*, 96, 114102. doi: 10.1103/PhysRevLett.96.114102
14. Sporns, O., and Betzel, R.F. (2016). Modular brain networks. *Annu. Rev. Psychol.*, 67, 613-640. doi: 10.1146/annurev-psych-122414-033634
15. Wildie, M., and Shanahan, M. (2012). Metastability and chimera states in modular delay and pulse-coupled oscillator networks. *Chaos*, 22, 043131. doi: 10.1063/1.4766592
16. Blondel, V.D., Guillaume, J.L., Lambiotte, R., and Lefebvre, E. (2008). Fast unfolding of communities in large networks. *J. Stat. Mech. Theor. Exp.*, 10, P10008. doi: 10.1088/1742-5468/2008/10/P10008
17. Clauset, A., Newman, M.E.J., and Moore, C. (2004). Finding community structure in very large networks. *Phys. Rev. E*, 70, 066111. doi: 10.1103/PhysRevE.70.066111
18. Duch, J., and Arenas, A. (2005). Community detection in complex networks using extremal optimization. *Phys. Rev. E*, 72, 027104. doi: 10.1103/PhysRevE.72.027104
19. Girvan, M., and Newman, M.E.J. (2002). Community structure in social and biological networks. *PNAS*, 99, 7821–7826. doi: 10.1073/pnas.122653799
20. Guimerà, R., and Amaral, L.A.N. (2005). Functional cartography of complex metabolic networks. *Nature*, 433, 895–900. doi: 10.1038/nature03288
21. Newman, M.E.J. (2004). Fast algorithm for detecting community structure in networks. *Phys. Rev. E*, 69, 066133. doi: 10.1103/PhysRevE.69.066133
22. Newman, M.E.J., and Girvan, M. (2004). Finding and evaluating community structure in networks. *Phys. Rev. E*, 69, 026113. doi: 10.1103/PhysRevE.69.026113
23. Hastie, T., Tibshirani, R., and Friedman, J. (2009). *The Elements of Statistical Learning*. Vol. 2. New York City, NY: Springer.
24. Berens, P., Keliris, G.A., Ecker, A.S., Logothetis, N.K., and Tolias, A.S. (2008). Feature selectivity of the gamma-band of the local field potential in primate primary visual cortex. *Front. Neurosci.*, 2, 199-207. doi: 10.3389/neuro.01.037.2008
25. Frien, A., Eckhorn, R., Bauer, R., Woelbern, T., and Kehr, H. (1994). Stimulus-specific fast oscillations at zero phase between visual areas V1 and V2 of awake monkey. *Neuroreport*, 5, 2273-2277. doi: 10.1097/00001756-199411000-00017

26. MacKay, W.A., and Mendonca, A.J. (1995). Field potential oscillatory bursts in parietal cortex before and during reach. *Brain Res.*, 704, 167-174. doi: 10.1016/0006-8993(95)01109-9
27. Murthy, V.N., and Fetz, E.E. (1992). Coherent 25- to 35-Hz oscillations in the sensorimotor cortex of awake behaving monkeys. *PNAS*, 89, 5670-5674. doi: 10.1073/pnas.89.12.5670
28. Rougeul, A., Bouyer, J.J., Dedet, L., and Debray, O. (1979). Fast somato-parietal rhythms during combined focal attention and immobility in baboon and squirrel monkey. *Electroencephalogr. Clin. Neurophysiol.*, 46, 310-319. doi: 10.1016/0013-4694(79)90205-0
29. Sanes, J., and Donoghue, P. (1993). Oscillations in local field potentials of the primate motor cortex during voluntary movement. *PNAS*, 90, 4470-4474. doi: 10.1073/pnas.90.10.4470
30. Stetson, C., and Andersen, R.A. (2014). The parietal reach region selectively anti-synchronizes with dorsal premotor cortex during planning. *J. Neurosci.*, 34, 11948-11958. doi: 10.1523/JNEUROSCI.0097-14.2014
31. Vaidya, M., Kording, K., Saleh, M., Takahashi, K., and Hatsopoulos, N.G. (2015). Neural coordination during reach-to-grasp. *J. Neurophysiol.*, 114, 1827-1836. doi: 10.1152/jn.00349.2015
32. Weiss, A.R., Gillies, M.J., Philastides, M.G., Apps, M.A., Whittington, M.A., et al. (2018). Dorsal anterior cingulate cortices differentially lateralize prediction errors and outcome valence in a decision-making task. *Front. Hum. Neurosci.*, 22:307. doi: 10.3389/fnhum.2018.00203
33. Womelsdorf, T., Johnston, K., Vinck, M., and Everling, S. (2010). Theta-activity in anterior cingulate cortex predicts task rules and their adjustments following errors. *PNAS*, 107, 5248-5253. doi: 10.1073/pnas.0906194107
34. Leon, P.S., Knock, S.A., Spiegler, A., and Jirsa, V.K. (2015). Mathematical framework for large-scale brain network modeling in the virtual brain. *NeuroImage*, 111, 385-430. <https://doi.org/10.1016/j.neuroimage.2015.01.002>
35. FitzHugh, R. (1961). Impulses and physiological states in theoretical models of nerve membrane. *Biophys. J.*, 1, 445:466. [https://doi.org/10.1016/S0006-3495\(61\)86902-6](https://doi.org/10.1016/S0006-3495(61)86902-6)
36. Hindmarsh, J.L., and Rose, R.M. (1984). A model of neuronal bursting using three coupled first order differential equations. *Proceedings of the Royal Society of London. Series B. Biological Sciences*, 221, 87-102. doi: 10.1098/rspb.1984.0024
37. Izhikevich, E.M. (2003). Simple model of spiking neurons. *IEEE Transactions of Neural Networks*, 14, 1569-1572. doi: 10.1109/TNN.2003.820440
38. Nagumo, J., Arimoto, S., and Yoshizawa, S. (1962). An active impulse transmission line simulating nerve axon. *Proc. IRE*, 50, 2061-2070.
39. Rinzel, J. (1987). A Formal Classification of Bursting Mechanisms in Excitable Systems, in *Mathematical Topics in Population Biology, Morphogenesis, and Neurosciences*. E. Teramoto, M. Yamaguti (Eds.), Lecture notes in Biomath. Berlin: Springer, pp. 267-281.
40. Van der Pol, B. (1926). On relaxation-oscillations. *The London, Edinburgh and Dublin Phil. Mag. & J. of Sci.*, 2, 978-992. doi: <https://doi.org/10.1080/14786442608564127>
41. Jansen, B., and Rit, V. (1995). Electroencephalogram and visual evoked potential generation in a mathematical model of coupled cortical columns. *Biol. Cybern.*, 73, 357-366. doi: 10.1007/BF00199471
42. Stefanescu, R. and Jirsa, V. (2008). A low dimensional description of globally coupled heterogeneous neural networks of excitatory and inhibitory. *PLoS Comput. Biol.*, 4, 26-36. doi: <https://doi.org/10.1371/journal.pcbi.1000219>
43. Stefanescu, R., and Jirsa, V. (2011). Reduced representations of heterogeneous mixed neural networks with synaptic coupling. *Phys. Rev. E. Stat. Nonlin. Soft Matter Phys.* 83(2): 026204. doi: 10.1103/PhysRevE.83.026204
44. Wilson, H., and Cowan, J. (1972). Excitatory and inhibitory interactions in localized populations of model neurons. *Biophys. J.*, 12, 1-24. doi: 10.1016/S0006-3495(72)86068-5
45. Wilson, H., and Cowan, J. (1973). A mathematical theory of functional dynamics of cortical and thalamic nervous tissue. *Kybernetik*, 13, 55-80. doi: <https://doi.org/10.1007/BF00288786>
46. Wong, K. F., and Wang, X.J. (2006). A recurrent network mechanism of time integration in perceptual decisions. *J. Neurosci.*, 26, 1314-1328. doi: <https://doi.org/10.1523/JNEUROSCI.3733-05.2006>
47. Ghosh, A., Rho, Y., McIntosh, A.R., Kötter, R., and Jirsa, V.K.. "Noise during rest enables the exploration of the brain's dynamic repertoire." *PLoS computational biology* 4, no. 10 (2008): e1000196.
48. Deco, G., Kringelbach, M.L., Jirsa, V.K. and Ritter, P., 2017. The dynamics of resting fluctuations in the brain: metastability and its dynamical cortical core. *Scientific reports*, 7(1), pp.1-14.
49. Chialvo, D.R. (2010). Emergent complex neural dynamics. *Nature Phys.*, 6, 744-750. doi:10.1038/nphys1803
50. Hesse, J., and Gross, T. (2014). Self-organized criticality as a fundamental property of neural systems. *Front. Syst. Neurosci.*, 8, 166. doi: 10.3389/fnsys.2014.00166
51. Kohn, F.R.M., and Ritzmann, R. (2018). Gravity and neuronal adaptation, in vitro and in vivo-from neuronal cells up to neuromuscular responses: A first model. *Euro. Biophys. J.*, 47, 97-101. doi: <https://doi.org/10.1007/s00249-017-1233-7>
52. Yochum, M., Modolo, J., Mogul, D.J., Benquet, P., and Wendling, F. (2019). Reconstruction of post-synaptic potentials by reverse modeling of local field potentials. *J. Neural. Eng.*, 16(2): 026023. doi: 10.1088/1741-2552/aafbfb
53. Frey, S.H., Funnell, M.G., Gerry, V.E., and Gazzaniga, M.S. (2005). A dissociation between the representation of tool-use skills and hand dominance: Insights from left- and right-handed callosotomy patients. *J. Cogn. Neurosci.*, 17, 262-272. doi: 10.1162/0898929053124974
54. Gonzalez, C.L.R., Ganel, T., and Goodale, M.A. (2006). Hemispheric specialization for the visual control of action is independent of handedness. *J. Neurophysiol.*, 95, 3496-3501. doi: 10.1152/jn.01187.2005

55. Meador, K.J., Loring, D.W., Lee, K., Hughes, M., Lee, G., et al. (1999). Cerebral lateralization: Relationship of language and ideomotor praxis. *Neurology*, 53, 2028-2031. doi: 10.1212/wnl.53.9.2028
56. Perenin, M.T., and Vighetto, A. (1988). Optic ataxia: A specific disruption in visuomotor mechanisms. I. Different aspects of the deficit in reaching for objects. *Brain*, 111, 643-674. doi: 10.1093/brain/111.3.643
57. Radoeva, P.D., Cohen, J.D., Corballis, P.M., Lukovits, T.G., and Koleva, S.G. (2005). Hemispheric asymmetry in a dissociation between the visuomotor and visuo-perceptual streams. *Neuropsychologia*, 43, 1763-1773. doi: 10.1016/j.neuropsychologia.2005.02.005
58. Smutok, M.A., Grafman, J., Salazar, A.M., Sweeney, J.K., Jonas, B.S., et al. (1989). Effects of unilateral brain damage on contralateral and ipsilateral upper extremity function in hemiplegia. *Phys. Ther.*, 69, 195-203. doi: 10.1093/ptj/69.3.195
59. Izhikevich, E. (2007). *Dynamical Systems In Neuroscience*. MIT Press, Cambridge, MA.
60. Grefkes, C., and Fink, G.R. (2005). The functional organization of the intraparietal sulcus in humans and monkeys. *J. Anat.* 207, 3-17. doi: 10.1111/j.1469-7580.2005.00426.x
61. Ishida, H., Fornia, L., Grandi, L.C., Umiltà, M.A., and Gallese, V. (2013). Somato-motor haptic processing in posterior inner perisylvian region (SII/pIC) of the macaque monkey. *PLoS ONE*, 8, doi: 10.1371/journal.pone.0069931
62. Walton, M.E., and Mars, R.B. (2008). Probing human and monkey anterior cingulate cortex in variable environments. *Cogn. Affect. Behav. Neurosci.*, 7, 413-422. doi: 10.3758/cabn.7.4.413
63. Nakamura, H., Kuroda, T., Wakita, M., Kusunoki, M., Kato, A., et al. (2001). From three-dimensional space vision to prehensile hand movements: The lateral intraparietal area links the area V3A and the anterior intraparietal area in macaques. *J. Neurosci.*, 21, 8174-8187. doi: <https://doi.org/10.1523/JNEUROSCI.21-20-08174.2001>
64. Bakola, S., Gamberini, M., Passarelli, L., Fattori, P., and Galletti, C. (2010). Cortical connections of parietal field Pec in the macaque: Linking vision and somatic sensation for the control of limb action. *Cereb. Cortex*, 20, 2592-2604. doi: <https://doi.org/10.1093/cercor/bhq007>
65. Bakola, S., Passarelli, L., Gamberini, M., Fattori, P., and Galletti, C. (2013). Cortical connectivity suggests a role in limb coordination for macaque area PE of the superior parietal cortex. *J. Neurosci.*, 33, 6648-6658. doi: <https://doi.org/10.1523/JNEUROSCI.4685-12.2013>
66. Gattass, R., Sousa, A.P., Mishkin, M., and Ungerleider, L.G. (1997). Cortical projections of area V2 in the macaque. *Cereb. Cortex*, 7, 110-129. doi: 10.1093/cercor/7.2.110
67. Marusic, U., Meeusen, R., Pisot, R., and Kavcic, V. (2014). The brain in micro- and hypergravity: The effects of changing gravity on the brain electrocortical activity. *Eur. J. Sport Sci.*, 14(8), 813-822. doi: 10.1080/17461391.2014.908959
68. Greicius, M.D., Supekar, K., Menon, V., and Dougherty, R.F. (2009). Resting-state functional connectivity reflects structural connectivity in the default mode network. *Cereb. Cortex*, 19, 72-78. doi: 10.1093/cercor/bhn059
69. Margulies, D.S., Vincent, J.L., Kelly, C., Lohmann, G., Uddin, L.Q., et al. (2009). Precuneus shares intrinsic functional architecture in humans and monkeys. *Proc. Natl. Acad. Sci. USA*, 106, 20069-20074. doi: 10.1073/pnas.0905314106
70. Leech, R., Kamourieh, S., Beckmann, C.F., Sharp, D.J. (2011). Fractionating the default mode network: Distinct contributions of the ventral and dorsal posterior cingulate cortex to cognitive control. *J. Neurosci.*, 31, 3217-3214. doi: 10.1523/JNEUROSCI.5626-10.2011
71. Corbetta, M., Patel, G., and Shulman, G.L. (2008). The reorienting system of the human brain: From environment to theory of mind. *Neuron*, 58, 306-324. doi: 10.1016/j.neuron.2008.04.017
72. Vincent, J.L., Kahn, I., Snyder, A.Z., Raichle, M.E., Buckner, R.L. et al. (2008). Evidence for a frontoparietal control system revealed by intrinsic functional connectivity. *J. Neurophysiol.*, 100, 3328-3342. doi: 10.1152/jn.90355.2008
73. Seeley, W.W., Menon, V., Schatzberg, A.F., Keller, J., Glover, G.H., et al. (2007). Dissociable intrinsic connectivity networks for salience processing and executive control. *J. Neurosci.*, 27, 2349 – 2356. doi: 10.1523/JNEUROSCI.5587-06.2007
74. Leech, R., Braga, R., and Sharp, D.J. (2012). Echoes of the brain within the posterior cingulate cortex. *J. Neurosci.*, 32, 215-222. doi: 10.1523/JNEUROSCI.3689-11.2012
75. Leech, R., and Sharp, D.J. (2014). The role of the posterior cingulate cortex in cognition and disease. *Brain*, 137, 12-32. doi: 10.1093/brain/awt162
76. Battaglia-Mayer, A., Ferraina, S., Genovesio, A., Marconi, B., Squatrito, S. et al. (2001). Eye-hand coordination during reaching. II. An analysis of the relationships between visuomanual signals in parietal cortex and parieto-frontal association projections. *Cereb. Cortex*, 11, 528-544. doi: 10.1093/cercor/11.6.528
77. Ferraina, S., Battaglia-Mayer, A., Genovesio, A., Marconi, B., Onorati, P., et al. (2001). Early coding of visuomanual coordination during reaching in parietal area Pec. *J. Neurophysiol.*, 85, 462-467. doi: 10.1152/jn.2001.85.1.462
78. Vitis, M.D., Breveglieri, R., Hadjidimitrakakis, K., Vanduffel, W., Galletti, C., et al. (2019). The neglected medial part of the macaque area PE: Segregated processing of reach depth and direction. *Brain Struct. Funct.*, 224, 2537-2557. doi: <https://doi.org/10.1007/s00429-019-01923-8>
79. Zeki, S.M. (1967). Visual deficits related to size of lesion in prestriate cortex of optic chiasm sectioned monkeys. *Life Sci.*, 6, 1627-1638. doi: 10.1016/0024-3205(67)90173-7
80. Van Asselen, M., Kessels, R.P., Neggers, S.F., Kappelle, L.J., Frijns, C.J., et al. (2006). Brain areas involved in spatial working memory. *Neuropsychologia*, 44, 1185-1194. doi: 10.1016/j.neuropsychologia.2005.10.005
81. Anguera, J.A., Reuter-Lorenz, P.A., Willingham, D.T., and Seidler, R.D. (2010). Contributions of spatial working memory to visuomotor learning. *J. Cogn. Neurosci.*, 22, 1917-1930. doi: 10.1162/jocn.2009.21351
82. Cunningham, H.A. (1989). Aiming error under transformed spatial mappings suggests a structure for visual-motor maps. *J. Exp. Psychol. Hum. Percept. Perform.*, 15, 493-506. doi: 10.1037//0096-1523.15.3.493

83. Cerri, G., Shimazu, H., Maier, M.A., and Lemon, R.N. (2003). Facilitation from ventral premotor cortex of primary motor cortex outputs to macaque hand muscles. *J. Neurophysiol.*, 90, 832–842. doi: 10.1152/jn.01026.2002
84. Fogassi, L., Gallese, V., Buccino, G., Craighero, L., Fadiga, L., et al. (2001). Cortical mechanism for the visual guidance of hand grasping movements in the monkey: A reversible inactivation study. *Brain*, 124, 571-586. doi: 10.1093/brain/124.3.571
85. Gentilucci, M., Scandolara, C., Pigarev, I.N., and Rizzolatti, G. (1983). Visual responses in the postarcuate cortex (area 6) of the monkey that are independent of eye position. *Exp. Brain Res.*, 50, 464-468. doi: 10.1007/BF00239214
86. Murata, A., Fadiga, L., Fogassi, L., Gallese, V., Raos, V., et al. (1997). Object representation in the ventral premotor cortex (area F5) of the monkey. *J. Neurophysiol.*, 78, 2226-2230. doi: 10.1152/jn.1997.78.4.2226
87. Umiltà, M.A., Brochier, T., Spinks, R.L., and Lemon, R.N. (2007). Simultaneous recording of macaque premotor and primary motor cortex neuronal populations reveals different functional contributions to visuomotor grasp. *J. Neurophysiol.*, 98, 488-501. doi: 10.1152/jn.01094.2006
88. Dum, R.P., and Strick, P.L. (2005). Frontal lobe inputs to the digit representations of the motor areas on the lateral surface of the hemisphere. *J. Neurosci.*, 25, 1375-1386. doi: 10.1523/JNEUROSCI.3902-04.2005
89. Matsumura, M., and Kubota, K. (1979). Cortical projection to hand-arm motor area from post-arcuate area in macaque monkeys: A histological study of retrograde transport of horseradish peroxidase. *Neurosci. Lett.*, 11, 241-246. doi: 10.1016/0304-3940(79)90001-6
90. Matelli, M., Camarda, R., Glickstein, M., and Rizzolatti, G. (1986). Afferent and efferent projections of the inferior area 6 in the macaque monkey. *J. Comp. Neurol.*, 251, 281-298. doi: 10.1002/cne.902510302
91. Muakkassa, K.F., and Strick, P.L. (1979). Frontal lobe inputs to primate motor cortex: Evidence for four somatotopically organized 'premotor' areas. *Brain Res.*, 177, 176-182. doi: 10.1016/0006-8993(79)90928-4
92. Kandel, E.R., Schwartz, J.H., and Jessell, T.M. (2000). *Principles of Neural Science*. New York, NY: McGraw-Hill
93. Bridge, H., Bell, A.H., Ainsworth, M., Sallet, J., Premereur, E., et al. (2019). Preserved extrastriate visual network in a monkey with substantial, naturally occurring damage to primary visual cortex. *eLife*, 8:e42325. doi: <https://doi.org/10.7554/eLife.42325>
94. Huff, T., Mahabadi, N., and Tadi, P. (2021). *Neuroanatomy, visual cortex*. In: *StatPearls [Internet]*. Treasure Island, FL: StatPearls Publishing. doi: <https://www.ncbi.nlm.nih.gov/books/NBK482504/>
95. Leon, P.S., Knock, S.A., Woodman, M.M., Domide, L., Mersmann, J., McIntosh, A.R., et al. (2013). The virtual brain: A simulator of primate brain network dynamics. *Front. in Neuroinform.*, 7:10. doi: 10.3389/fninf.2013.00010
96. Kötter, R., (2004). Online retrieval, processing, and visualization of primate connectivity data from the CoCoMac Database. *Neuroinformatics*, 2, 127-144. doi: 10.1385/NI:2:2:127
97. Kötter, R., and Wanke, E. (2005). Mapping brains without coordinates. *Philos. Trans. R. Soc. Lond. B Biol. Sci.*, 360, 751–766. doi: 10.1098/rstb.2005.1625
98. Bakker, R., Wachtler, T., and Diesmann, M. (2012). Cocomac 2.0 and the future of tract-tracing databases. *Front. Neuroinform.*, 6:30. doi: 10.3389/fninf.2012.00030
99. Stephan, K.E., 2013. The history of CoCoMac. *Neuroimage*, 80, pp.46-52.
100. Aboitiz, F. (1992). Brain connections: Interhemispheric fiber systems and anatomical brain asymmetries in human. *Biol. Res.*, 25, 51-61. PMID: 1365702
101. Hugdahl, K. (2005). Symmetry and asymmetry in the human brain. *European Review*, 13, 119-133. doi: 10.1017/S1062798705000700
102. Corballis, M.C. (2017). The evolution of lateralized brain circuits. *Front. Psych.*, 8, 1021. doi: 10.3389/fpsyg.2017.01021
103. Toga, A.W., Narr, K.L., Thompson, P.M., and Luders, E. (2009). "Brain Asymmetry: Evolution," in *Encyclopedia of Neuroscience*, ed L.R. Squire (Cambridge, MA: Academic Press), 303-311.
104. Castiello, U. and Begliomini, C., 2008. The cortical control of visually guided grasping. *The Neuroscientist*, 14(2), pp.157-170.
105. Culham, J.C., Danckert, S.L., De Souza, J.F., Gati, J.S., Menon, R.S. and Goodale, M.A., 2003. Visually guided grasping produces fMRI activation in dorsal but not ventral stream brain areas. *Experimental brain research*, 153(2), pp.180-189.
106. Nelissen, K. and Vanduffel, W., 2011. Grasping-related functional magnetic resonance imaging brain responses in the macaque monkey. *Journal of Neuroscience*, 31(22), pp.8220-8229.
107. Freud, E., Plaut, D.C. and Behrmann, M., 2016. 'What'is happening in the dorsal visual pathway. *Trends in Cognitive Sciences*, 20(10), pp.773-784.
108. Rubinov, M. and Sporns, O., 2010. Complex network measures of brain connectivity: uses and interpretations. *Neuroimage*, 52(3), pp.1059-1069.
109. Freeman, L.C., 1977. A set of measures of centrality based on betweenness. *Sociometry*, pp.35-41.
110. Liu, J., Li, M., Pan, Y., Lan, W., Zheng, R., W, F.X., et al. (2017). Complex brain network analysis and its applications to brain disorders: A survey. *Complexity*, 2017, ID: 8372741
111. Bavelas, A., 1950. Communication patterns in task-oriented groups. *The journal of the acoustical society of America*, 22(6), pp.725-730.
112. Mira, C. (1997). Chua's circuit and the qualitative theory of dynamic systems. *J. Franklin. Inst.*, 334B, 737-744.
113. Firmin, L., Field, P., Maier, M.A., Kraskov, A., Kirkwood, P.A., et al. (2014). Axon diameters and conduction velocities in the macaque pyramidal tract. *J. Neurophysiol.*, 112, 1229-1240. doi:10.1152/jn.00720.2013
114. Olson, C.R., Musil, S.Y., and Goldberg, M. (1993). Posterior cingulate cortex and visuospatial cognition: Properties of single neurons in behaving monkey. *J. Neurophysiol.*, 76, 3285-3300. doi: 10.1007/978-1-4899-6704-6_1
115. Ray, S., Hsiao, S.S., Crone, N.E., Franaszczuk, P.J., and Niebur, E. (2008). Effect of stimulus intensity on the spike-local field potential relationship in the secondary somatosensory cortex. *J. Neurosci.*, 28, 7334-7343. doi: <https://doi.org/10.1523/JNEUROSCI.1588-08.2008>

116. Smuda J, Klein CA, Murayama Y, Steudel T, Krampe E, Oeltermann A, Werner J, Logothetis NK and Evrard H (2019). Local field potential activity in the macaque anterior insular cortex. *Front. Neurosci. Conference Abstract: 12th National Congress of the Belgian Society for Neuroscience*. doi: 10.3389/conf.fnins.2017.94.00021

117. Choi, H., and Mihalas, S. (2019). Synchronization dependent on spatial structure of a mesoscopic whole-brain network. *PLoS Comp. Biol.*, 15(4): e10006978. doi: <https://doi.org/10.1371/journal.pcbi.1006978>

118. Cocchi, L., Gollo, L.L., Zalesky, A., and Breakspear, M. (2017). Criticality in the brain: A synthesis of neurobiology, models, and cognition. *Prog. In Neurobiol.*, 158, 132-152. doi: <https://doi.org/10.1016/j.pneurobio.2017.07.002>

119. Bezdek J.C., 1981. *Pattern Recognition with Fuzzy Objective Function Algorithms*. Plenum Press, New York

Figures

Figure 1

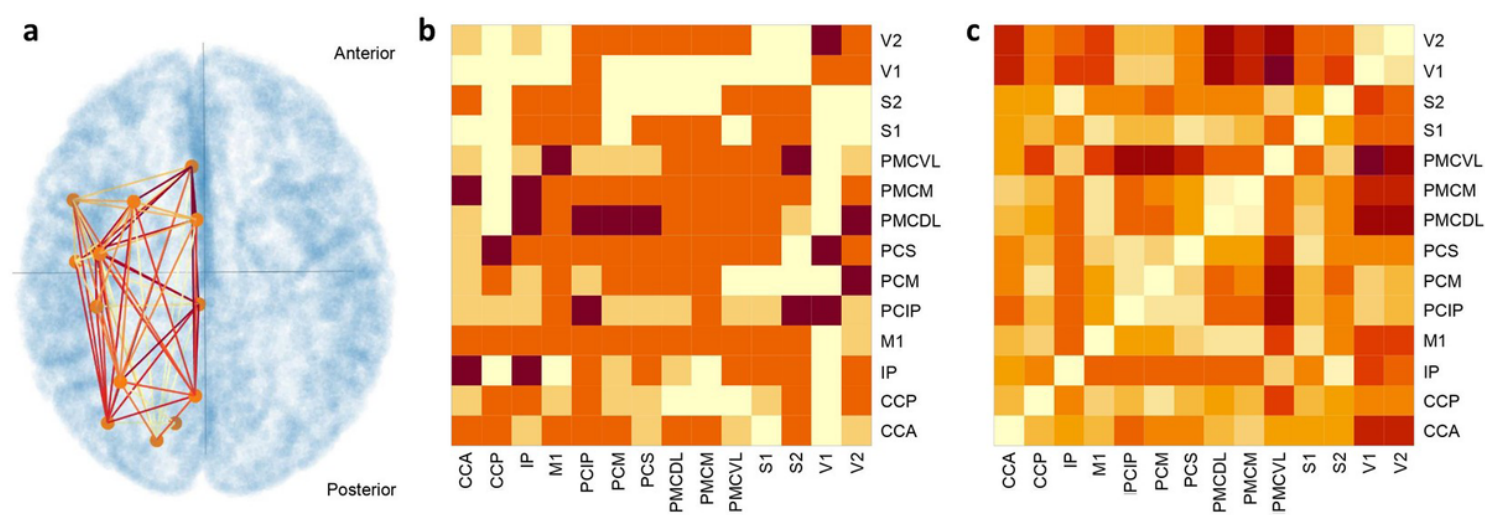


Figure 1

Visuomotor module. **a.** A static three-dimensional image of brain regions (nodes) and interconnections (edges) encapsulated by TVB default cortical surface, illustrating the visuomotor module that resulted from passing the primate connectome to the modularity algorithm. Orange nodes represent the 14 brain regions present in the visuomotor module. Orange-to-red colored edges represent the 146 connections between those nodes. Orientation of brain aspect is superior-to-inferior along the axial plane, with anterior-to-posterior direction being top to bottom. Orange-to-red color encoding is used to help delineate between which edges connect what nodes. Reciprocal and recursive connections are not explicitly visualized for clarity. However, they are included in the dataset, which can be seen in the tract-weight matrix in **b.** **b.** 14 x 14 square tract-weight matrix. This matrix is a weighted, directed graph. **c.** 14 x 14 square tract-length matrix. This matrix is a weighted, undirected graph.

Figure 2

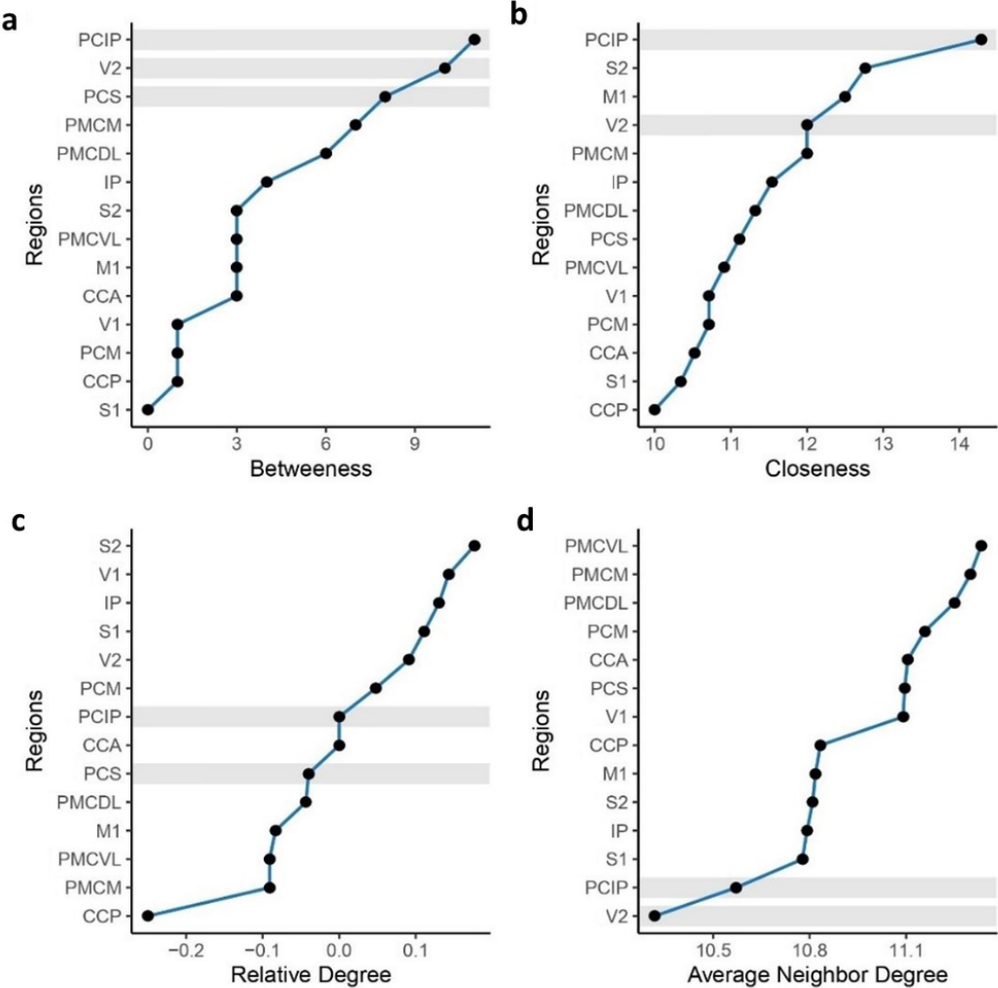


Figure 2

Local network analysis of visuomotor module criticalities and resiliency. **a**Betweenness measure of visuomotor module suggesting the PCIP, V2, and PCS are network centralities. **b**. Closeness measure of visuomotor module suggesting the PCIP and V2 are network centralities. **c**. Relative degree measure of visuomotor module suggesting the PCIP and PCS are network centralities. For relative degree, regions with a relative degree at or around 0 were considered the highest scoring regions as these regions have equal numbers of incoming and outgoing connections, making them most susceptible to both perturbations by incoming connections and perturbing downstream nodes through outgoing connections. In **a**, **b**, and **c**, the nodes that had centrality measures in the top 25% in more than one metric are highlighted. Thus, PCIP is considered the primary centrality of the visuomotor module, whereas PCS and V2 are considered secondary centralities. **d**.Average neighbor degree measure of visuomotor module suggesting V2 and PCIP are regions that if perturbed, injured, or otherwise change their activity have the highest potential to compromise visuomotor-network function and therefore behavior. The three centralities identified from the local network analysis were cross-referenced with the 25% of nodes scoring lowest on the resilience measure.

Figure 3

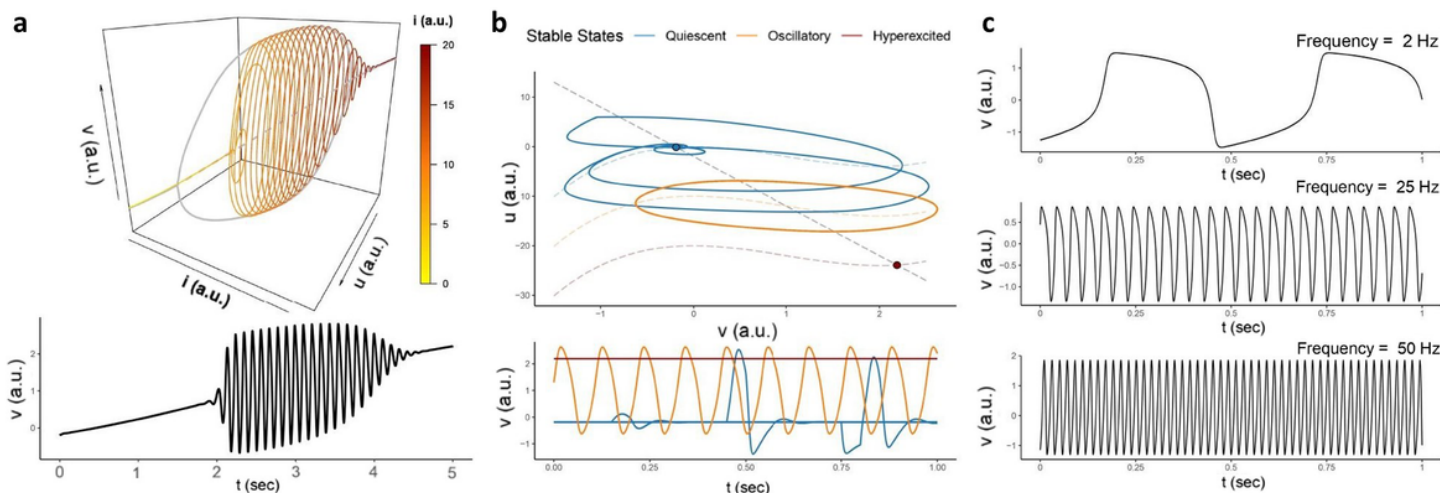


Figure 3

Exploration of brain-region model using the qualitative theory of dynamic systems. **a top.** A three-dimensional bifurcation analysis of the brain-region model with two schemes: a steady-state bifurcation scheme and an instantaneous bifurcation scheme. The bifurcation analysis shows the model goes through three main types of criticalities leading to a bifurcation, a nodular stable attractor, a supercritical Hopf bifurcation leading to a limit cycle attractor, as well as a subcritical Hopf bifurcation leading again to a stable nodular attractor. However, the instantaneous bifurcation analysis appears to experience a hysteretic effect; its bifurcations lag behind the steady-state criticality points. **a bottom.** The time-series voltage data of the ramping procedure. **b top.** This 2D phase plane illustrates the primary activity regimes of the brain-region model. The model has a quiescent/excitabile regime, an oscillatory regime, as well as a hyperexcited regime, which is the result of the shifting nullcline. The respective time-series voltage data is depicted in **b bottom.** **c.** Although phenomenological and fairly simplistic, the brain-region model can produce a wide range of frequencies in the physiological range for macroscopic LFP recordings. With selected parameterizations from the tabulated parameter data, the brain-region model produces oscillatory activity in the 2, 25, and 50 Hz range, which corresponds to delta, alpha, and gamma waves.

Figure 4

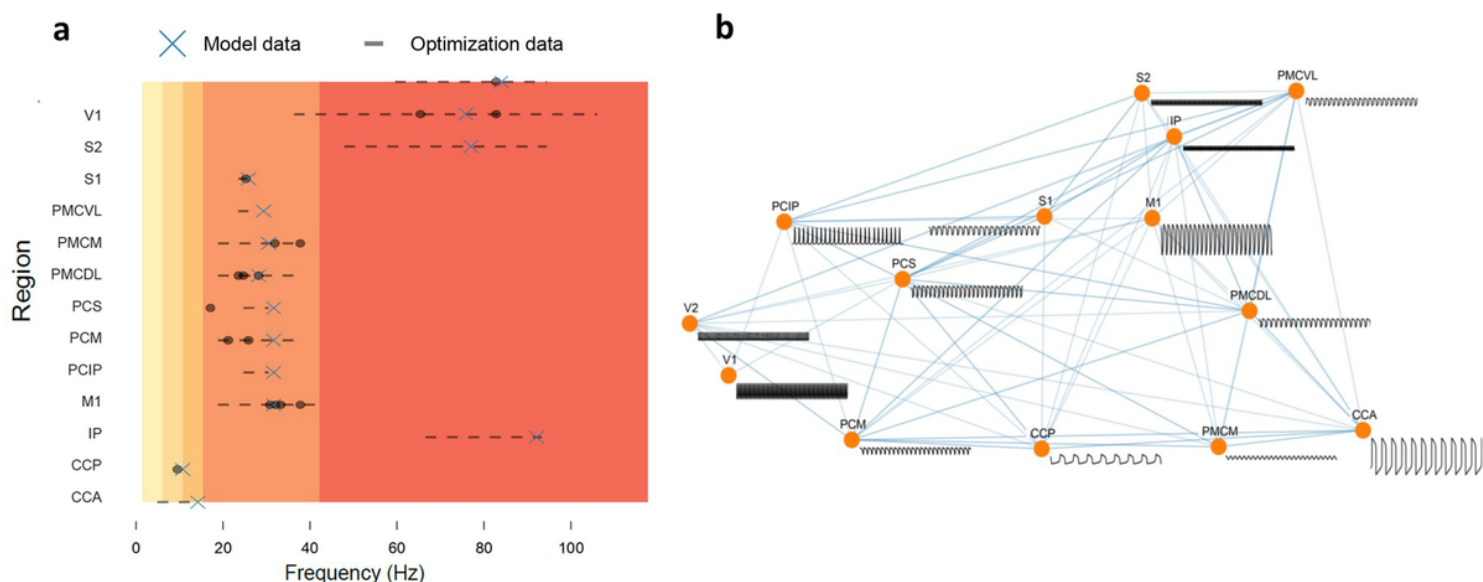


Figure 4

Visuomotor NNE model in 1G. **a.** Tuning of the NNE model to 1G data acquired from the literature of monkeys and humans performing reach-to-grasp-like visuomotor movement. Black dotted lines and black dots indicate frequency ranges and dominant frequencies, respectively, reported in the literature. Blue X's represent the LFP activity of the model in frequency space with a global coupling constant of $g = 0.0055$, showing the model's ability to produce LFP activity in a subnetwork underlying or controlling visuomotor movement as animals do in 1G. **b.** 2D representation of structural visuomotor subnetwork and corresponding time-series LFP data produced by each brain region in the model.

Figure 5

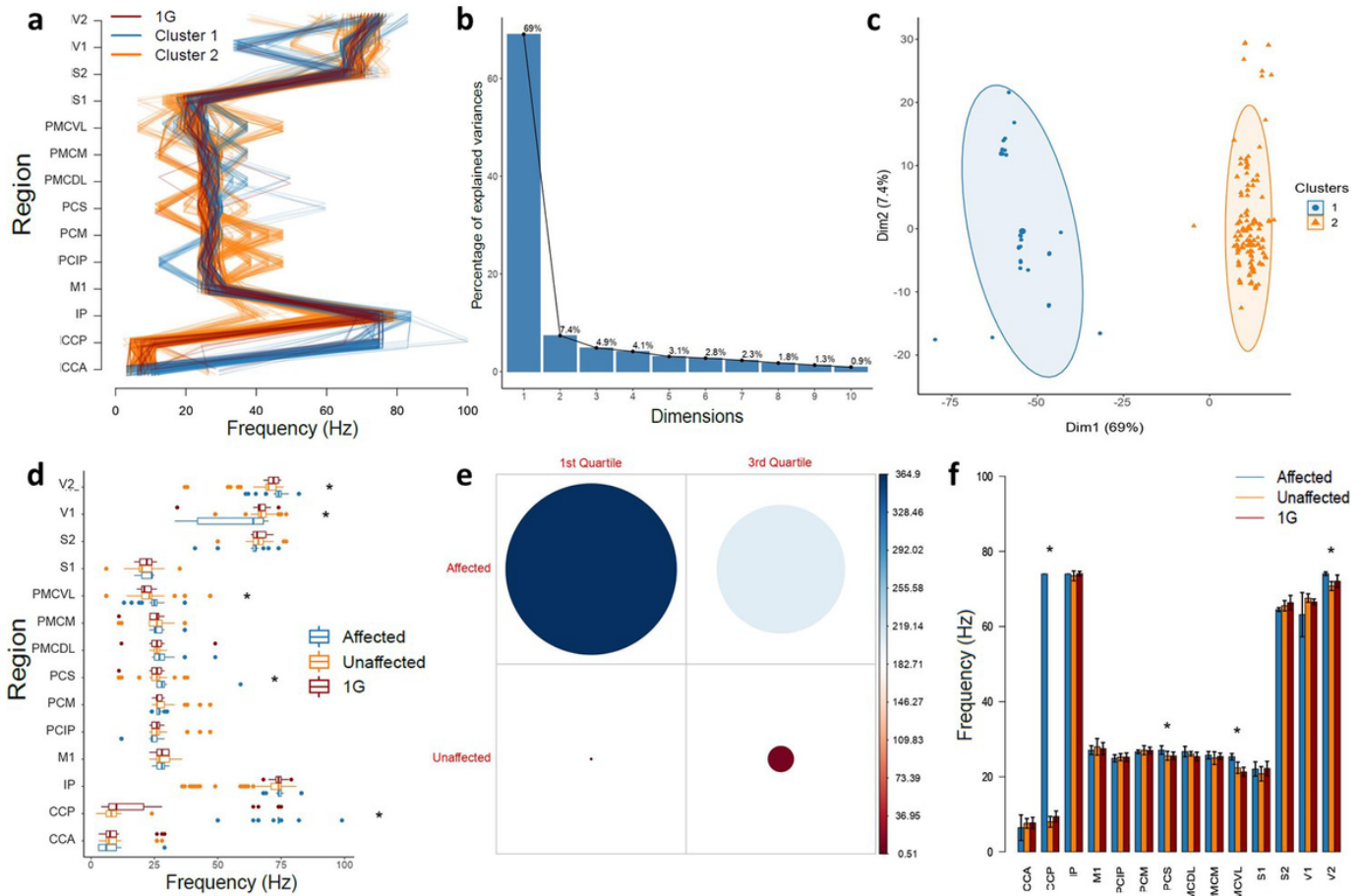


Figure 5

Analysis of visuomotor model subjected to hypogravity. **a**. Soft k-means clustering of 1G (red) and hypogravity frequency data from NNNE model (cluster 1, blue; cluster 2, orange). Each simulation passed to the soft k-means algorithm is depicted region-wise in frequency space. **b**. Dimensional reduction using PCA expressing the percentage of explained variance of the data as a function of resulting principal components. **c**. Reduced visualization of soft k-means clustering, projected onto the PCA first and second dimensions. **d**. Box-and-whisker plot of region-wise NNNE model frequency data. Qualitative distribution analysis, comparing each cluster's IQR to that of the known 1G data, identifies clusters 1 and 2 as the hypogravity-affected (blue) and -unaaffected groups (orange), respectively. Known 1G data is red. Moreover, marked distribution shifts when comparing the hypogravity-affected and -unaaffected groups suggest the neural activity of V2, V1, PMCVL, PCS, and CCP are altered in hypogravity, where the oscillatory frequencies of V2, PMCVL, PCS, and CCP increase and V1 decreases. These regions are denoted with asterisks. **e**. Size-encoded heatmap quantifying the distribution shifts between clusters and known 1G data using RMS to calculate the error between the 1st and 3rd quantiles. When compared to the known 1G data, cluster 1 (1st quantile, RMS = 364.90 Hz; 3rd quantile, RMS = 204.85 Hz) has a much greater error than cluster 2 (1st quantile, RMS = 0.51 Hz; 3rd quantile, RMS = 8.67 Hz). Thus, this quantification supports the qualitative distribution analysis; cluster 1 is designated the hypogravity-affected group, and cluster 2 is designated the hypogravity-unaaffected group. **f**. Qualitative analysis of mean NNNE model frequency data. When comparing mean shifts of the hypogravity-affected group to the mean and standard deviations of the hypogravity-unaaffected group, V2, PMCVL, PCS, and CCP show large changes in mean activity (denoted with asterisks). These regions, as well as the direction of change (increase in mean frequency when subjected to hypogravity), agree with the box-and-whisker plot analysis.

Figure 6

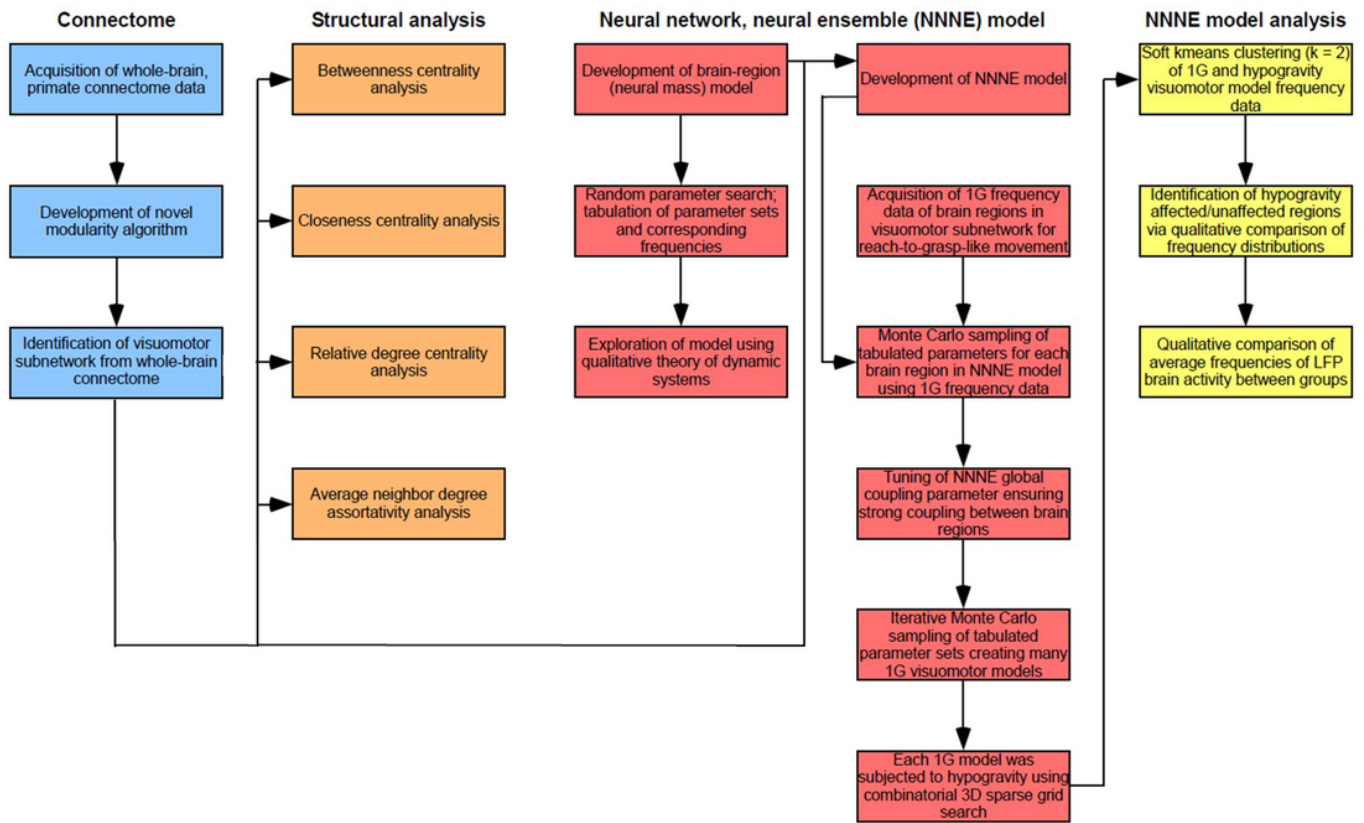


Figure 6

Computational and analytical workflow. Moving column-wise from left to right, the workflow diagram begins with the connectomic work completed, including the development of the modularity algorithm utilized to identify the visuomotor subnetwork. This connectomic column leads to the structural analysis of the visuomotor subnetwork, determining which brain regions are structurally important with respect to subnetwork activity. This structural work, with the development of a brain-region or neural mass model, is a predicate on top of which the NNNE model is developed and tuned. The resulting data from simulations of 1G NNNE models subjected to a hypogravity framework is clustered using an unsupervised machine learning approach, qualitatively analyzed to determine hypogravity-affected and -unaffected brain regions.

Figure 7

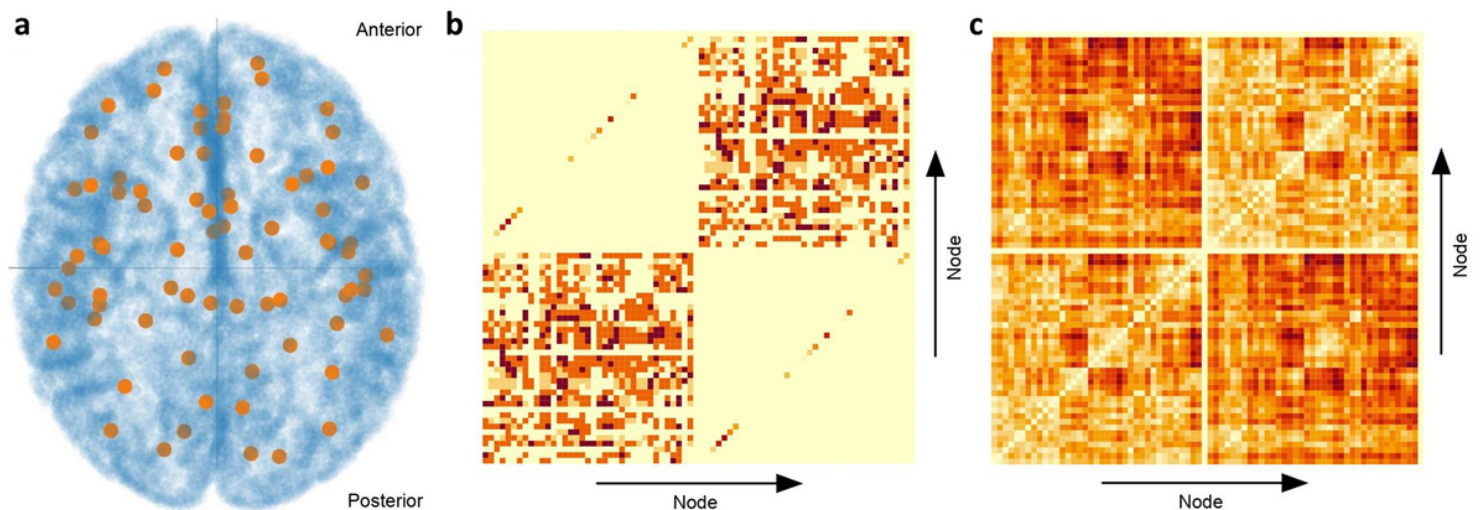


Figure 7

Primate connectome. **a.** A static three-dimensional image of brain regions (nodes) encapsulated by TVB default cortical surface, illustrating the diffuse spatiality and granularity of nodes throughout the brain (1,560 interregional connections not shown for visual clarity). Orange nodes represent the 76 brain regions present in the connectivity dataset. Orientation of brain aspect is superior-to-inferior along the axial plane, with the anterior-to-posterior direction being top to bottom. **b.** A 76 x 76 square tract-weight matrix with main diagonal from bottom left to top right. This matrix represents a weighted, undirected graph between the first and fourth quadrants representing symmetric connections between hemispheres. The second and third quadrants represent interconnectivity within respective hemispheres and are identical to one another. **c.** A 76 x 76 square tract-length matrix. This non-symmetric matrix represents a weighted, directed graph.

Figure 8

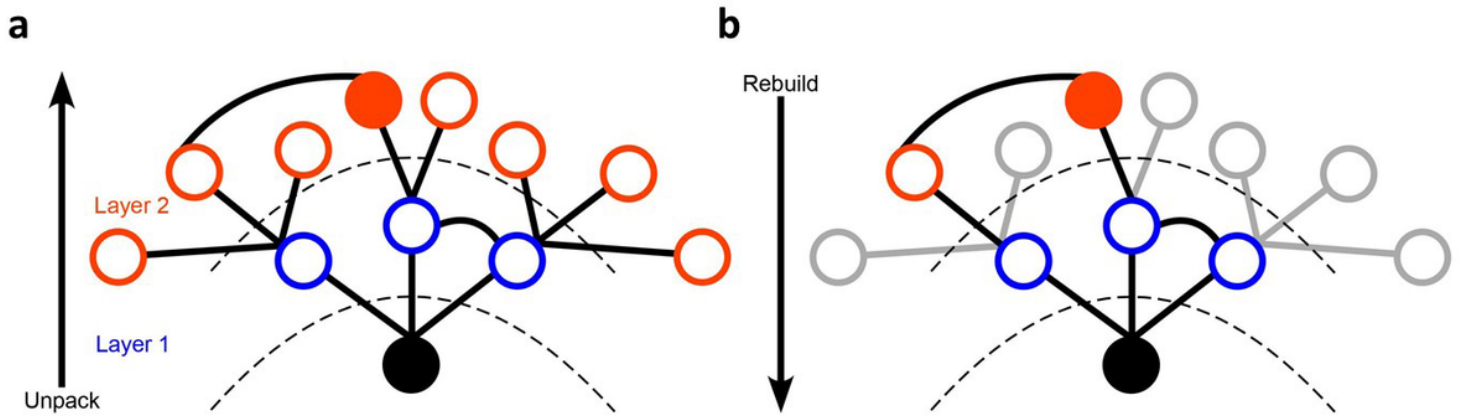


Figure 8

A conceptual framework of modularity algorithm. **a.** Diagrammatic description of the unpacking procedure. The algorithm begins at the output node (black node; M1) and unpacks layers of the connectome (first layer of blue-outlined nodes and second layer of orange-outlined nodes) until the algorithm finds the input node (solid orange node; V1). Layers are considered all the nodes that impinge on the node being considered. Here and in implementation, the algorithm unpacks two layers of source nodes. **b.** Diagrammatic description of the rebuilding procedure. Once the algorithm detects the input node, the algorithm self-constrains by only considering the input node's targets (here, the property of self-constraining is depicted by grey-outlined nodes in layer 2), tracing all possible paths back to the output node, again constrained by the number of steps the algorithm can take along paths. The resulting non-greyled, colored nodes and connections would comprise the module.

Supplementary Files

This is a list of supplementary files associated with this preprint. Click to download.

- [Appendix.docx](#)